DOI 10.2478/ama-2024-0029

STUDY OF CONTACT ALGORITHMS INFLUENCING SPECIMEN RESPONSE IN NUMERICAL SIMULATION OF DYNAMIC COMPRESSION TEST

Paweł BARANOWSKI*, Krzysztof DAMAZIAK*

*Military University of Technology, Faculty of Mechanical Engineering, Institute of Mechanics and Computational Engineering, 2 Gen. S. Kaliskiego Street, 00-908 Warsaw, Poland

pawel.baranowski@wat.edu.pl, krzysztof.damaziak@wat.edu.pl

received 11 August 2023, revised 15 Septemeber 2023, accepted 26 Septemeber 2023

Abstract: This paper demonstrates the importance of a proper contact algorithm selection when a constitutive model is correlated and validated, especially in the case of brittle materials. A parametric study is carried out to study the influence of contact parameters on the outcomes of the numerical simulations of a dynamic compression test. The split Hopkinson pressure bar (SHPB) model is developed, and sandstone rock is considered as a representative material having considerably different properties compared to SHPB bars. The finite element method (FEM) and smoothed particle hydrodynamics (SPH) were used to simulate specimen behaviour using a LS-Dyna solver. Two contact types based on the penalty method are analysed: nodes to surface (FEM and SPH) and surface to surface (FEM only). Furthermore, three approaches of contact stiffness calculation are used for each contact type. The waveform data and failure patterns are then compared among all simulated cases and the corresponding experimental outcomes. It is found that the soft constraint stiffness (*SOFT = 1)* provides the best outcomes, especially in the case of one-way contact, and is nearly insensitive to stiffness scaling parameters. By contrast, standard (*SOFT* = 0) and segment-based (*SOFT* =2) approaches require a substantial effort in adjusting the stiffness scaling parameters to obtain satisfactory results. This paper provides valuable guidance for correlating and validating parameters of constitutive models for rock and other brittle materials in the SHPB test.

Key words: JH-2 constitutive model, sandstone, rock, SHPB, LS-DYNA

1. INTRODUCTION

Brittle materials, such as concrete, rocks or ceramics, have been extensively studied over the last years (1-11) (1, 2, 11, 3–10). In the case of dynamic problems, two main loadings scenarios can be distinguished: blast and dynamic impacts. The scholars mainly investigate the engineering structures of various applications made of these materials using experimental techniques (12–16). However, over the last two or three decades the numerical modelling has been found to be very effective in supporting the laboratory and field tests (17–21). The credibility of the computational simulations depends on an efficient numerical model that provides a reproduction of a simulated phenomenon as close as possible to the real-world data.

One of the basic experiments to investigate the dynamic brittle material properties is the split Hopkinson pressure bar (SHPB) test, which generates a high strain rate compression loading (22, 23). The mechanical properties of various types of brittle materials have been widely investigated using the SHPB setup. These studies include rocks (24–26), concrete (10, 27, 28), glass (29) or ceramics (30). Considering the complexity of the dynamic conditions to which the tested material is subjected, numerical methods are extremely useful for providing better insights in the material behaviour and associated failure processes during the SHPB test. However, a high-fidelity constitutive modelling and a validated numerical model are needed to provide information that will be useful for the understanding of material failure phenomena. Notably, the SHPB setup is a first-choice experiment to be reproduced using numerical tools to correlate the selected constitutive model in dynamic conditions, which is then used in subsequent simulations of a material subjected to complex dynamic loadings such as blasts or impacts. The selected constants of a constitutive model, usually responsible for strength enhancement and damage, are modified and adjusted until a proper correlation with failure pattern of the specimen (31–34) waveform data, consisting of stress vs. strain curve and/or transmitted and reflected pulses (23, 35, 36), is achieved. Certainly, physical properties of the material described using specific constants of the constitutive model affect the results. However, other elements can also drastically influence the response of a discretised material specimen, among which the mesh properties and simulations parameters should be mentioned. These data are usually described in the referenced papers; however, many of the studies do not show detailed information about the numerical models in terms of the contact modelling as the sample-bar interface conditions can heavily affect obtained results, a situation similar to the case of real-world tests. General information regarding contact type or friction properties is not enough since the numerical procedures responsible for contact calculations can have a drastic impact on the numerical simulation outcomes.

Compared with previous studies of SHPB numerical simulations of concrete, rock or other brittle materials (23, 31, 40, 41, 32–39), the scientific and novel aspect of this paper includes a detailed presentation of contact parameters' effect on the brittle specimen response in the SHPB numerical simulations. Thus, the presented paper aims to fill the abovementioned gap between the correlation of constitutive model parameters and verification of

other aspects of numerical modelling, including especially contact definition. Due to the interlinks mentioned above, the lack of such information raises questions about the validity of the derived constitutive parameters. The numerical simulations are based on the SHPB methodology presented earlier (27, 42). During experimental tests a lubricant and polyester foil were used between the specimen and the bars to minimise friction; thus, it was neglected both in calculations and theoretical problem description. To make conclusions more general, two different numerical techniques are used for the study: Finite Element Method (FEM) and Smoothed Particle Hydrodynamics (SPH). Both methods are utilised to simulate rock behaviour, but from the point of view of the algorithms describing a continuum, these methods are completely different (see Sections 2.2 and 2.3). For the both methods, the Johnson–Holmquist ceramics (JH-2) model proposed by Timothy Johnson and Gordon Holmquist (4, 8, 43–50) was used, which has been widely adopted to simulate various dynamic loading problems (4, 7, 43–48). The parameters have been determined for a selected sandstone using a methodology presented in previous papers (42, 51). The model was validated under various stress conditions using the simulations of single-elemental tests, SHPB test, drop-weight impact tests, blast tests and projectile impact tests. The results of these simulations are not included in this study and they will be available in a forthcoming publication (52). The present study mainly aimed to demonstrate a need to correlate both constitutive model and contact procedure parameters, because both of these have a significant impact on the obtained numerical results.

The remainder of this article is structured as follows. In Section 2, the problem is formulated and the numerical modelling, including theoretical backgrounds of the FEM and SPH methods, contact definitions and constitutive model parameters as well as simulated cases, are described; Section 3 presents the study's results and their discussion, where the waveform data and failure patterns are analysed for different contact parameters; and Section 4 presents the conclusions.

2. PROBLEM DESCRIPTION

The SHPB setup is a very popular experimental test used to evaluate mechanical properties of materials under dynamic conditions and it is widely used in correlation and/or validation of the selected constitutive model for simulated material. Therefore, the authors decided to investigate the problem of the contact parameters' influence on the results based on this setup to highlight the importance of not restricting the tuning-up to parameters of the constitutive model only. The numerical studies are conducted using the commercially available explicit LS-Dyna code. The choice was made based on the popularity of this particular code among researchers modelling SHPB tests. At the same time, contact procedures implemented in LS-Dyna are representative of the algorithms used in a majority of software packages based on FEM that are named as a numerical simulation tool in articles presenting investigations on rock-like materials. Especially, contact procedure steering parameters are typical (although they can have different names).

This section also contains a short description of the numerical techniques underlying the presented research. Since the theory of these techniques is well-known, the authors provide only the brief, vital information, supported by widely accepted references.

2.1. SHPB setup and model definition

To achieve this goal, a representative numerical model of the real-world SHPB setup was developed. In the actual SHPB apparatus, the following main components can be distinguished: an air gun system; incident, transmitted and striker bars; velocity measurement system; and data acquisition system. The three bars were made of steel C45 and had diameters of 40.0 mm. During tests, a lubricant and polyester foil were used to minimise friction between the bars and the specimen as much as possible. The effectiveness of this concept has already been demonstrated in previous studies (42, 53).

In all simulated cases, it was decided to model a full 3D SHPB setup with the correspondent conditions with the experiments, with the following assumptions:

- The simulated test procedure is highly dynamic in its nature; thus, the analyses were conducted within time domain (transient analyses) using explicit time integration scheme with the implementation of an explicit LS-Dyna commercial hydrocode with multiparallel processing (MPP) (54–57).
- Only the bars with the specimen inserted between them were assumed while developing the finite element (FE) model based on the experimental setup. The other components were not included in the numerical modelling. Furthermore, to initialise a stress wave in the incident bar, a pressure load corresponding to the incident wave from the experiments was applied.
- The bars were represented using fully integrated hexagonal elements with a mesh size of 1.0 mm at the bar ends interacting with the specimen, while a larger element size was adopted for the remaining parts of the incident and transmission bars.
- As stated before, the specimen was modelled using two approaches: FEM and SPH. For both methods, the same grid size was considered, i.e. the average size of FE and the distance between the particles equal to 1.0 mm.
- The friction plays a significant role in FE predictions of the material response in SHPB tests. However, frictionless interaction was assumed between the bars and the specimen since polyester foil and lubricant were used in the SHPB experiments.

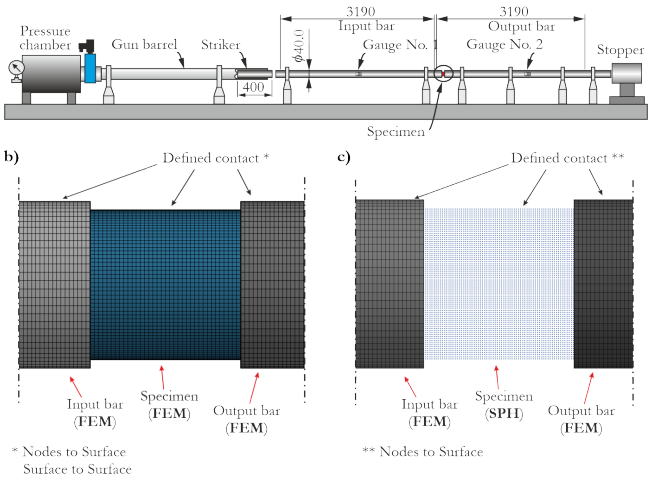

Fig. 1. (a) Scheme of the experimental SHPB setup and corresponding numerical model with (b) FEM specimen ann (c) SPH specimen

The laboratory setup and corresponding numerical models with Lagrangian and SPH representations of the specimen are presented in Fig. 1.

2.2. FEM modelling

In the field of solid mechanics, displacement-based FEM is currently the most widely used tool for solving Partial Differential Equations (PDEs). This comes from a few features characterising this method and the fact that its development was parallel in time with the rapid growth of computer hardware capabilities. The very basic idea of the method, which is to change PDE into a system of linear equations, allows us to adopt linear algebra techniques to obtain an approximate solution to the given problem. Easy algorithmising of linear algebra routines allowed development of robust and very efficient software packages. Increasingly easier access to hardware capable of handling real-live problems made this technique the most popular tool for engineering analysis. The FEM, as a very mature and popular method, has an extraordinarily rich bibliography. Starting with the classic work of Zienkiewicz (58), one can also mention the detailed lecture by Bathe (59), and many others (60–62). The governing equation of displacement FEM is the weak form of the minimum total potential energy principle:

$$\delta\Pi = \int_\Omega \delta\varepsilon^T \sigma \mathrm{d}\Omega - \int_\Omega \delta\mathbf{u}^T \mathbf{b}\mathrm{d}\Omega$$
$$\int_\Gamma \delta\mathbf{u}^T \mathbf{F}\,\mathrm{d}\Gamma + \int_\Omega \rho\delta\mathbf{u}^T \ddot{\mathbf{u}}\mathrm{d}\Omega = 0 \quad (1)$$

where Ω denotes the volume of the body, Γ the surface of the body, F the vector of external forces acting on a body, u the displacement vector, b the vector of mass forces (acting on specific volume), σ the stress tensor, ε the strain tensor and Π the total energy of a body.

The solution of Eq. (1) indicates that one must find the displacement vector of all nodes (deformed shape of a body) fulfilling the equation. To solve the equation using FEM, the domain Ω (body of interest) is divided into subdomains (elements), connected to each other at corners (nodes). The movement of each corner within the subdomain is related to the movement of other corners via known, predefined, functions (shape functions). All these steps follow the idea of the Ritz method (63) and are required to approximate the integra-differential equation Eq. (2) by the system of algebraic equations that can be presented in matrix form as follows:

$$\mathbf{M}\ddot{\mathbf{u}} + \mathbf{D}\dot{\mathbf{u}} + \mathbf{K}\mathbf{u} = \mathbf{F} \quad (2)$$

where M denotes the mass matrix, D the damping matrix and K the stiffness matrix.

Time integration of Eq. (2) is conducted using the central difference method utilising the following differential operators:

$$\ddot{\mathbf{u}}^n = \frac{1}{\Delta t^n}(\dot{\mathbf{u}}^{n+1} - \dot{\mathbf{u}}^{n-1}) \quad (3)$$

$$\dot{\mathbf{u}}^{n+\frac{1}{2}} = \frac{1}{\Delta t_{n+\frac{1}{2}}}(\mathbf{u}^{n+1} - \mathbf{u}^n) \quad (4)$$

In the central difference method only a diagonal matrix of mass is inverted, which is one of the major advantages of this method.

2.3. SPH modelling

Despite its popularity, FEM has its limitations. Loss of material continuity, multi-scaling, large distortion of elements and high gradients variation are on the top of such difficulties. Therefore, new methods capable of overcoming these problems are constantly sought and developed. One such new method, or rather family of methods, is the meshless approach. As the name suggests, the biggest advantage of these methods is a lack of mesh. Probably the oldest of the meshless methods is SPH.

SPH is a meshfree method that originated in 1977 for astrophysics applications. A detailed description of SPH is shown in the study of Gingold and Monaghan (64), as well as in the study of Liu and Gu (65) and that of Liu and Liu (66), to mention the most popular sources. In short, description of continuum with the SPH uses conservation equations of mass, momentum end internal energy as the governing equations:

$$\frac{d\rho}{dt} = -\rho\frac{\partial v_i}{\partial x_i}; \quad \frac{dv_i}{dt} = \frac{1}{\rho}\frac{\partial \sigma_{ij}}{\partial x_j}; \quad \frac{dE}{dt} = \frac{\sigma_{ij}}{\rho}\frac{\partial v_i}{\partial x_j} \quad (5)$$

where s denotes stress, v velocity, ij indexes of components and E internal energy.

Eqs. (5) are solved by interpolation of a given value of function <f> (i.e., density, velocity, energy, etc.) in a given point based on the known value of this function in surrounding points (particles) using the following formula:

$$< \mathrm{f} > (\mathbf{x}_p) = \sum_{q=1}^{N} \mathrm{f}(\mathbf{x}_q)\mathrm{W}(\mathbf{x}_p - \mathbf{x}_q, h)\ \Delta V_q \quad (6)$$

where <f> denotes the function, x the vector defining particle position, p,q the indexes denoting different particles, W the kernel function and h the maximum distance between particles (smoothing length). Application of Eq. (6) to the laws of conservation leads to the following set of equations that constitute the set of basic equations used to model continuum with SPH:

$$\frac{\partial \rho_p}{\partial t} = \sum_{q=1}^{N} m_q v_{pq} \frac{\partial W_{pq}}{\partial x_p},$$
$$\frac{\partial v_p}{\partial t} = \sum_{q=1}^{N} m_q \left(\frac{\sigma_p}{\rho_p^2} + \frac{\sigma_q}{\rho_q^2}\right)\frac{\partial W_{pq}}{\partial x_p}, \quad (7)$$
$$\frac{\partial E_p}{\partial t} = \sum_{q=1}^{N} m_q \frac{\sigma_p \sigma_q}{\rho_p \rho_q} v_{pq} \frac{\partial W_{pq}}{\partial x_p}.$$

where *m* denotes the mass of particle and *N* the number of particles within smoothing length.

In the presented simulations, the Lagrangian type of kernel W was used (i.e., representation of the function is formulated in material coordinates and thus the number of particles within the support domain is constant). Furthermore, the bulk viscosity coefficients were set as *Q1* = 1.5 and *Q2* = 1.0, since default values for the artificial bulk viscosity are not appropriate when SPH particles are used in such dynamic problems as the SHPB compression test (67, 68).

2.4. Constitutive modelling

The bars were assumed to have elastic properties of steel with the following properties: E_{steel} = 210 GPa, ν_{steel} = 0.3 and ρ_{steel} = 7,850 kg/m3. The sandstone rock was simulated using the JH-2 model with the parameters determined using single-element tests, followed by structural simulations of quasi-static and dynamic tests characterised by different loading conditions and stress

state complexities. The results of these simulations are not included in this study and they will be available in a forthcoming publication (52). The JH-2 parameters that were determined for the sandstone are presented in Tab. 1.

Tab. 1. Material properties for the JH-2 constitutive model for sandstone

Parameter	Value	Unit
Density, ρ	2350.0	kg/m^3
Poison's ratio, v	0.21	-
Bulk modulus, K_1	3735.6	MPa
Shear modulus, G	2686.0	MPa
Elastic modulus, E	6500.0	MPa
Hugoniot elastic limit, HEL	1982.0	MPa
HEL pressure, P_{HEL}	1374.0	MPa
Maximum tensile strength*, T	8.0	MPa
Intact strength coefficient, A	0.71	-
Fractured strength coefficient, B	0.30	-
Strain rate coefficient, C	0.022	-
Intact strength exponent, N	0.55	-
Fractured strength exponent, M	0.40	-
Bulk factor, β	1.0	-
Damage coefficient, D_1	0.002	-
Damage coefficient, D_2	1.20	-
Pressure coefficient 2, K_2	9000.0	MPa
Pressure coefficient 3, K_3	22000.0	MPa
Maximum normalised fracture strength, σ^*_{max}	0.25	-

*Value should be adjusted based on mesh size.

2.5. Contact modelling

Numerical procedures responsible for resolving the so-called contact problem work independently of the procedures responsible for finding a solution for the governing problem of a given numerical method (e.g., in case of FEM, displacement field fulfilling principle of minimum potential energy and thus state of equilibrium between external and internal forces). The outcome of contact procedures is comprised of forces acting between interacting bodies and kinematic contact conditions. In the solution of equilibrium problem, the former are treated as additional external load and the latter as additional support (additional boundary conditions).

In its essence, most of the contact algorithms used today are based on two most principal elements: procedures evaluating the distance between contacting bodies and procedures responsible for calculating contact forces. While there are many variations of the above, their outcome is directly responsible for the results of contact simulation. Detailed descriptions of contact procedures can be found in the literature (69–71).

Although several kinds of contact kinematics procedure are discussed in the literature, all of them rely on the tools provided by differential geometry to ascertain the distance between a point on one body and the projection of this point on an opposite body. In the classical implementation, the user must distinguish two contacting bodies by pointing out the so-called "master body" and "slave body". Then pairs of points on the "slave" and corresponding areas (called segments) on the "master" are found. Once such a pair is found, the distance between the point belonging to the slave body and its projection on the segment belonging to the master body is found. Schematics of the problem are shown in Fig. 2, where rs denotes a point on the slave body, Γ_m is the segment on the master body and ρ is the perpendicular projection of r_s on Γ_m.

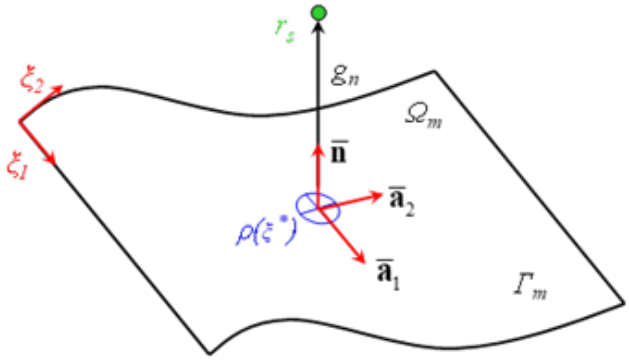

Fig. 2. Scheme of the contact problem in numerical codes

The projection point of the current position of r_s is defined as:

$$\frac{r_S-\rho(\bar{\xi}_{\square 1},\bar{\xi}_{\square 2})}{\|r_S-\rho(\bar{\xi}_{\square 1},\bar{\xi}_{\square 2})\|}\cdot\bar{\mathbf{a}}_\alpha(\bar{\xi}_{\square 1},\bar{\xi}_{\square 2})=0 \tag{8}$$

where α = 1,2; $\bar{\mathbf{a}}_\alpha(\bar{\xi}_{\square 1},\bar{\xi}_{\square 2})$ are the tangent covariant base vectors at projection point:

$$\bar{\mathbf{a}}_1=\left.\frac{\partial\rho(\xi^*)}{\partial\xi_{\square 1}}\right|_{\xi_{\square 1}=\xi^*_{\square 1},\xi_{\square 2}=\xi^*_{\square 2}}$$

$$\bar{\mathbf{a}}_2=\left.\frac{\partial\rho(\xi^*)}{\partial\xi_{\square 2}}\right|_{\xi_{\square 1}=\xi^*_{\square 1},\xi_{\square 2}=\xi^*_{2}} \tag{9}$$

Knowing the position of r_s and ρ allows us to define the distance between them and thus the distance between a point on the slave body and the surface of the master body:

$$g_N=[r_s-\rho(\xi^*)]\cdot\bar{\mathbf{n}} \tag{10}$$

where $\bar{\mathbf{n}}$ refers to the normal to the master face Γ_m at point ρ:

$$\bar{\mathbf{n}}=\frac{\bar{\mathbf{a}}_1\times\bar{\mathbf{a}}_2}{\|\bar{\mathbf{a}}_1\times\bar{\mathbf{a}}_2\|} \tag{11}$$

Knowing the distance g_N contact kinematic procedure allows us to define the kinematic contact conditions, as the following: $g_N = 0$ denotes contact, $g_N > 0$ no contact and $g_N < 0$ penetration.

The above approach can be used in a few different ways. When the contact kinematics procedure follows the above description, it is called a "node to segment" approach, sometimes also denoted as a "one-way contact treatment". The other often-used approach is to apply the above procedure twice, changing slave with master. These kinds of algorithms are called "surface to surface" or "two-way treatment". Finally, in the approach called "segment to segment", areas of potential contact are selected on both contact bodies, and then auxiliary points are created on these segments and the distance between the segments is evaluated using each of these auxiliary points.

In the second stage of the solution of the contact problem, contact forces are determined. This can be done under the assumption that the following conditions are fulfilled on the contact surface:

$$g_N \geq 0; \quad \sigma_N \leq 0; \quad g_N \sigma_N = 0 \tag{12}$$

where g_N denotes the distance between the contacting bodies, and σN the normal contact stress.

Such conditions define optimality conditions known as Karush-Kuhn-Tucker (KKT) conditions. These are necessary and sufficient conditions for a local minimum in nonlinear programming problems. In case of contact problem, optimisation is used to find contact forces fulfilling Eq. (12). Depending on how σ_N is calculated, several different methods of solving the contact problem are distinguished; among these, one of the most popular is the so-called penalty method, where the value of contact force in the given node is proportional to the value of the penetration of this node.

$$F_N = k_F g_N \tag{13}$$

where F_N denotes normal contact force, and k_F the penalty coefficient.

Eq. (13) clearly shows the concept of penalty function approach, but real-world implementations are slightly different. To help the procedure to find the optimum of the KKT problem, FEM programs usually calculate preliminary contact stiffness based on local stiffness of the numerical model and the user can adjust this preliminary value using correction coefficients. In the presented paper, the following three approaches of calculation of contact stiffness available in LS-Dyna software package are compared:

Normal stiffness derivation with SOFT = 0 (a representative equation for brick elements):

$$k_F = k_{Fnormal} = \frac{f_s K A^2}{V} \tag{14}$$

where f_s denotes the scaling factor (SLSFAC) provided by a user (0.1 is a default value), K the bulk modulus of the material of contacting elements, A the area of a segment and V the volume of element containing that segment.

Soft constraint stiffness derivation with SOFT =1.

An alternate way to calculate contact stiffness is to use the stability contact stiffness, k_{sp}, and the same is derived as follows:

$$k_{sp} = 0.5 \cdot f_{sp} \cdot m* \cdot \left(\frac{1}{\Delta t_c(t)} \right)^2 \tag{15}$$

where f_{sp} denotes the user-defined scaling factor (SOFSCL) for the SOFT = 1 formulation, $m*$ the function of the mass of the slave nodes and master nodes and Δt_c the initial time step.

Parameter k_{sp} is calculated based on masses of the nodes in contact and on the Courant's stability criterion of the maximum time step in transient explicit analyses. Then, the maximum value of the contact stiffness calculated using Eqs (14) and (15) is taken as follows:

$$k_{SOFT=1} = \max\left\{ k_{sp}, k_{Fnormal} \right\} \tag{16}$$

Segment-based stiffness derivation with *SOFT* = 2.

A third option is to apply a segment-based contact, which is similar to the soft constraint option with *SOFT* = 1; however, in this case, segment masses are used rather than nodal masses. Furthermore, when *SOFT* = 2 is activated, the dt is updated only when the solution time step grows by more than 5%. The stiffness in this case is calculated as follows:

$$k_{sp} = 0.5 \cdot f_s \cdot \left\{ \begin{matrix} SFS \\ \text{or} \\ SFM \end{matrix} \right\} \left(\frac{m_1 m_2}{m_1 + m_2} \right) \cdot \left(\frac{1}{\Delta t_c(t)} \right)^2 \tag{17}$$

where *SFS* and *SFM* denote scale factor on default slave and master penalty stiffness, respectively, and m_1 and m_2 the masses of the segments in contact.

Based on the aforementioned discussion, the application of contact stiffness parameters can be summarised as follows:

- *SFS* and *SFM* are the penalty scale factors of slave and master bodies to modify the contact stiffness.
- *SLSFAC* can scale up or down the contact stiffness, when *SOFT* = 0 or *SOFT* = 2 is used; therefore, the actual scale factor in these cases is the product of SFS or SFM and SLSFAC.
- *SOFSCL*, f_{SP}, the user defined scaling factor influences the contact stiffness only if *SOFT* = 1 is used and *SLS, SFM* and *SLSFAC* have no effect on the penalty contact stiffness.

In Tab. 2, a summary of the contact stiffness calculations using different approaches is shown. Based on these considerations, several cases using the numerical model of the SHPB setup with the FEM and SPH representation of the sandstone specimen were simulated (Section 2.6 can be referred to for more details) to analyse the influence of parameters of contact procedure on the obtained results.

Tab. 2. Summary of contact parameters available in LS-Dyna code

Type of contact	Contact stiffness formulation	SFS/ SFM	SLS FAC	SOF-SCL	Stiffness scaling factor calculation
Nodes to surface	SOFT = 0	+	+	-	SLSFAC*SFS/ SFM
	SOFT = 1	-	-	+	SOFSCL
	SOFT = 2	+	+	-	SLSFAC*SFS/ SFM
Surface to surface	SOFT = 0	+	+	-	SLSFAC*SFS/ SFM
	SOFT = 1	-	-	+	SOFSCL
	SOFT = 2	+	+	-	SLSFAC*SFS/ SFM

2.6. Description of contact parametric study

In the presented study, the influence of different contact kinematics algorithms (nodes to surface (NS), surface to surface (SS)) and different stiffness scaling parameters on the results of simulation of the dynamic compression test is analysed. Combinations of these parameters are summarised in detail in Tab. 3 and Tab. **4**.

For the FEM method, two types of contact were considered: NS and SS, whereas for the SPH method only the NS contact was employed.

In case of the NS contact (FEM and SPH), three main group of tests can be distinguished. In the first group, with the *SOFT* = 1 method of contact stiffness derivation, default values of *SLSFAC, SFS* and *SFM* were used since in this case they do not have any effect on the resultant stiffness. In this group of tests, the *SOFSCL* was modified in each test. Next, the *SOFT* = 0 method was analysed in two steps, in which the *SFS/SFM* were modified firstly, and the other parameters have the same values in each test,

which was then followed by the analysis of different values of *SLSFAC* while *SFS/SFM* = 0.3 and *SOFSCL* = 0 remained unchanged. As shown in Tab. 2, when *SOFT* = 0 is enabled, the actual stiffness scale factor is the product of *SFS/SFM* and *SLSFAC*; thus, different values of these parameters and the resultant stiffness values were studied and discussed.

Tab. 3. Contact stiffness parameters analysed in the SHPB setup using NS method for contact kinematics in FEM and SPH

Test no.	SOFT	SLSFAC	SOFSCL	SFS	SFM
NS_S1_1	1.0	Default 0.1 (no effect)	0.1	Default 1.0	Default 1.0
NS_S1_2			0.3		
NS_S1_3			0.5		
NS_S1_4			0.7		
NS_S1_5			1.0		
NS_S1_6			2.0		
NS_S1_7			5.0		
NS_S1_8			7.0		
NS_S0_1	0.0	Default 0.1	0.0 (no effect)	0.1	0.1
NS_S0_2				0.3	0.3
NS_S0_3				0.5	0.5
NS_S0_4				0.7	0.7
NS_S0_5				1.0	1.0
NS_S0_6				2.0	2.0
NS_S0_7				5.0	5.0
NS_S0_8				7.0	7.0
NS_S0_11	0.0	0.1	0.0 (no effect)	Default 1.0	Default 1.0
NS_S0_12		0.3			
NS_S0_13		0.5			
NS_S0_14		0.7			
NS_S0_15		1.0			
NS_S0_16		2.0			
NS_S0_17		5.0			
NS_S0_18		7.0			

In the case of SS contact, identical contact stiffness factors were used as for the cases presented in Tab. 3. However, two additional stages were also considered to study an effect of the *SOFT* = 2 option, with the same values of stiffness scale factors considered as in the simulations using NS contact. Therefore, with this option the parametric study of *SFS* and *SFM* values with the default *SLSFAC* was conducted, together with consideration of the fact of the study of *SLSFAC* and *SFS/SFM* remaining unchanged.

Tab. 4. Contact stiffness parameters analysed in the SHPB setup using SS method for contact kinematics in FEM

Test no.	SOFT	SLSFAC	SOFSCL	SFS	SFM
SS_S1_1	1.0	Default 0.1 (no effect)	0.1	Default 1.0	Default 1.0
SS_S1_2			0.3		
SS_S1_3			0.5		
SS_S1_4			0.7		
SS_S1_5			1.0		
SS_S1_6			2.0		
SS_S1_7			5.0		
SS_S1_8			7.0		
SS_S0_1	0.0	Default 0.1	0.0 (no effect)	0.1	0.1
SS_S0_2				0.3	0.3
SS_S0_3				0.5	0.5
SS_S0_4				0.7	0.7
SS_S0_5				1.0	1.0
SS_S0_6				2.0	2.0
SS_S0_7				5.0	5.0
SS_S0_8				7.0	7.0
SS_S0_11	0.0	0.1	0.0 (no effect)	Default 1.0	Default 1.0
SS_S0_12		0.3			
SS_S0_13		0.5			
SS_S0_14		0.7			
SS_S0_15		1.0			
SS_S0_16		2.0			
SS_S0_17		5.0			
SS_S0_18		7.0			
SS_S2_1	2.0	Default 0.1	0.0 (no effect)	0.1	0.1
SS_S2_2				0.3	0.3
SS_S2_3				0.5	0.5
SS_S2_4				0.7	0.7
SS_S2_5				1.0	1.0
SS_S2_6				2.0	2.0
SS_S2_7				5.0	5.0
SS_S2_8				7.0	7.0
SS_S2_11	2.0	0.1	0.0 (no effect)	Default 1.0	Default 1.0
SS_S2_12		0.3			
SS_S2_13		0.5			
SS_S2_14		0.7			
SS_S2_15		1.0			
SS_S2_16		2.0			
SS_S2_17		5.0			
SS_S2_18		7.0			

3. RESULTS AND DISCUSSION

3.1. Experimental SHPB tests

The representative stress–strain characteristics of the three tests with strain rates of 80 s−1, 110 s−1 and 240 s−1 are shown in Fig. 3a, for which the stress equilibrium in the specimen was achieved (Fig. 3b). For the purpose of the present study, the SHPB test with a middle strain rate of 110 s−1 was selected for studying the contact parameters' influence on the results. Fig. 3c presents waveform data, and Fig. 3d presents an exemplary specimen failure. Notably, these data were further used for analysis of the results in the present study.

The waveform data obtained in the SHPB experiment and numerical simulations were compared to analyse the influence of the contact parameters on the sandstone response. Both the transmitted and reflected characteristics represent a response of the tested material, since ultimately the stress vs. strain curve is directly obtained on their basis. Results are grouped with respect to different contact kinematics approaches (NS, SS). For each kinematics, the influence of the scaling factor of contact force is presented and discussed. The results are represented using waveform data, failure pattern and force values obtained for each case.

DOI 10.2478/ama-2024-0029

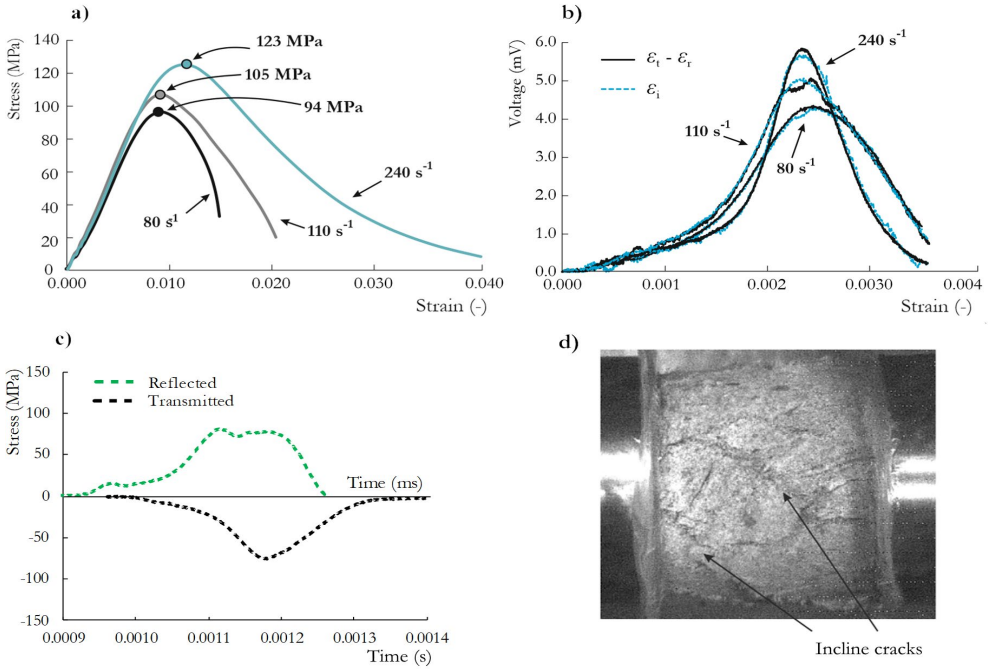

Fig. 3. Dynamic response of the sandstone tested using the SHPB setup; (a) stress vs. strain curves, (b) stress equilibria in three SHPB tests, (c) transmitted and reflected waves from the test at a strain rate of 110 s−1 and (d) representative specimen failure.

3.2. One-way contact (NS)

3.2.1. FEM: NS contact with SOFT = 1

In the first set of tests, the algorithm deriving contact stiffness was set to stabilise contact procedure (*SOFT* = 1). Results of the tests conducted using FEM for different values of the *SOFTSCL* parameter are shown in Fig. 4 and 5, presenting waveform data and specimen failure pattern, respectively. The stress response over time for different *SOFTSCL* values does not change drastically. There are some differences in the shape of transmitted wave, but they are not significant and can be treated as negligible. The very slight differences are noticeable starting from NS_S1_1 and continuing up until NS_S1_S5 for *SOFSCL* = 0.1 and 1.0, respectively. The values above 1.0 are inadmissible according to the LS-Dyna manual (54) and they yield the same results as if the *SOFTSCL* was set to 0.1 (or "0", which is a default value; and in fact, it gives 0.1). The same applies to the failure pattern of the specimen, which is nearly identical in all cases.

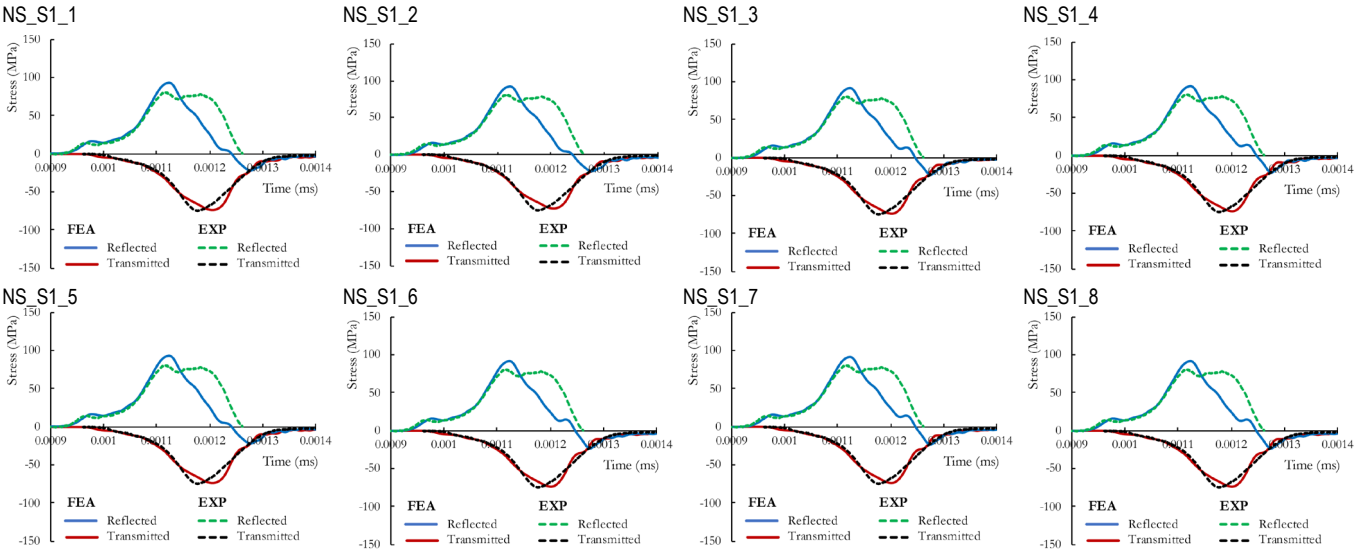

Fig. 4. Waveform data for FEM modelling of the sandstone in the SHPB test: influence of *SOFTSCL* using the *SOFT* = 1 in the NS contact definition

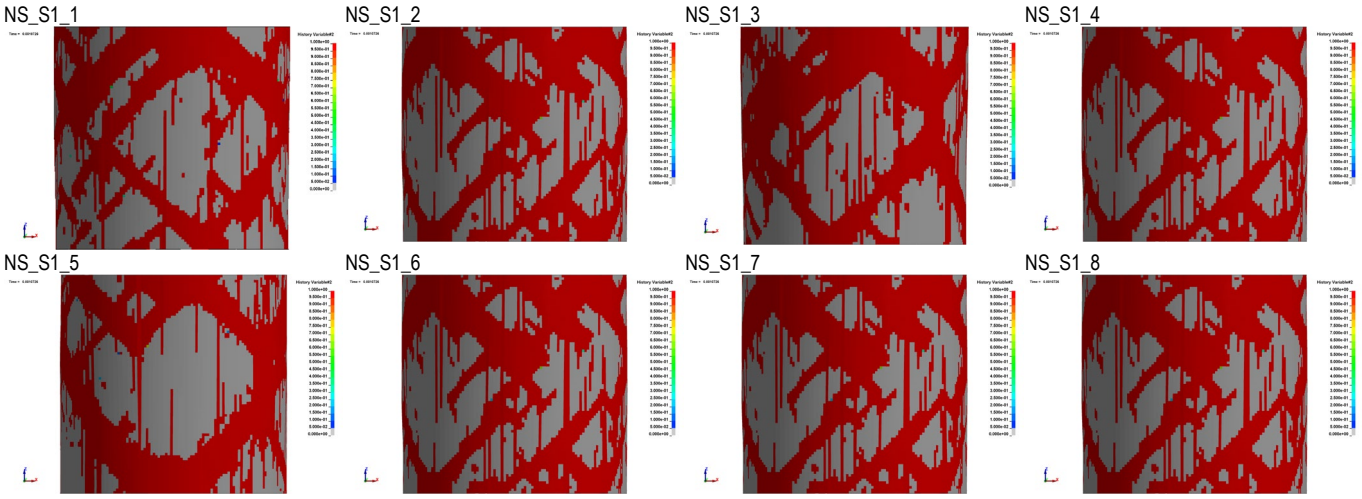

Fig. 5. Specimen failure patterns for FEM modelling of the sandstone in SHPB test: influence of *SOFTSCL* using the *SOFT* =1 in the NS contact definition

3.2.2. FEM: NS contact with SOFT = 0

In the second set of tests with FEM, the algorithm deriving contact stiffness was set to a default procedure of contact stiffness estimation (*SOFT* = 0). Results showing transmitted and reflected waves and failure pattern of the specimen for different values of *SFM/SFS* parameters are shown in Figs. 6 and 7, respectively. Unlike in the first set of tests, the influence of parameters controlling contact stiffness can be clearly observed. The waveform data of the first two tests can even be described as errors. Increasing the *SFS*/*SFM* scale factors resulted in a closer correlation between the numerical and experimental curves. However, for the first six cases, pronounced differences prevalent between numerically and experimentally obtained curves are noticeable. An overestimation and underestimation of the reflected and transmitted impulse, respectively, demonstrate that the stress equilibrium in the specimen was not achieved and the elastic wave was not correctly transferred by the specimen material dissipating in the sample. In other words, the impact force was too small due to insufficient contact stiffness between the specimen and the bars. Ultimately, from the series of eight numerical tests, only NS_S0_7 (*SFM/SFS* = 5.0) and NS_S0_8 (*SFM/SFS* = 7.0) show results similar to these obtained in the previous studies. However, in any case a proper reproduction of the real-world measurements was observed, especially in the case of reflected wave and its post-peak behaviour. The transmitted curve differs also from the experimental counterpart as well as numerical results with the *SOFT* = 1 presented in Fig. 5.

The abovementioned observations are reflected also in the incorrect failure patterns of the sandstone specimen (Fig. 7). Insufficient contact stiffness had a pronounced effect on the material failure. Starting from the NS_S0_1 and continuing up until NS_S0_7, an unsymmetrical failure represented by fully damaged elements can be observed within the top and bottom surfaces of the specimen. The first cases with the smallest values of *SFS/SFM* demonstrate the failure patterns that can be considered as numerical instabilities. When the contact stiffness increases, the failure starts to initiate at the boundaries of the specimen near the contact surfaces and for the *SFM/SFS* = 5.0 the cracking distribution starts to have a similar characteristic compared to the experimental outcome (Fig. 3d). Only for the last case are the results closer to the ones observed in the experiment, but the main drawback of the *SOFT* = 0 manifests in the cracking initiation (damage accumulation) within the specimen boundaries and edges. As a reminder, a lubricant and polyester foil were used between the specimen and the bars to minimise friction in the laboratory tests and consequently to drastically reduce lateral forces within the boundaries that could initiate cracks in the specimen.

The third series of numerical tests with the NS standard contact definition (*SOFT* = 0) involved the worst probable setup of contact parameters that would be used by less experienced users. The study consists of the cases with different values of *SLSFAC* included in the control contact card of the LS-Dyna package. Contrary to the cases with different values of *SFS/SFM* (Figs. 6 and 7), a less pronounced impact on the obtained results was observed here (Fig. 8 – waveform data and Fig. 9 – failure patterns). The worst reproduction of the reflected and transmitted curves was obtained for the first two cases, while the other six have a similar trend and correlation with the laboratory data. Nevertheless, the last four cases provide the best compliance with the experiment, but still the reflected wave with its post-peak behaviour was not correctly captured in any of the cases.

The failure patterns obtained from the simulations with *SOFT* = 0 and various *SLSFAC* are not so disturbed compared to the NS contact with different *SFS/SFM* stiffness values. The worst reproduction of the waveform data shown in Fig. 8 in the first two cases is also reflected in the specimen behaviour. The NS_S0_11 was characterised by a localised failure near the surfaces and edges of the specimen, while the NS_S0_12 demonstrated material failure at boundaries of the specimen and only a few horizontal cracks occurred within its length. A relatively symmetrical response of the specimen was observed with incline and horizontal cracks visible in the specimens starting from the *SLSFAC* = 0.5 (NS_S0_13) and continuing up until the last NS_S0_18 case. Unfortunately, despite well-captured failure patterns in most of the discussed cases (except the first two simulations), cracks started to initiate within the specimen boundaries and its edges, which is an undesirable and unphysical phenomenon, as discussed earlier.

Paweł Baranowski, Krzysztof Damiaziak

DOI 10.2478/ama-2024-0029

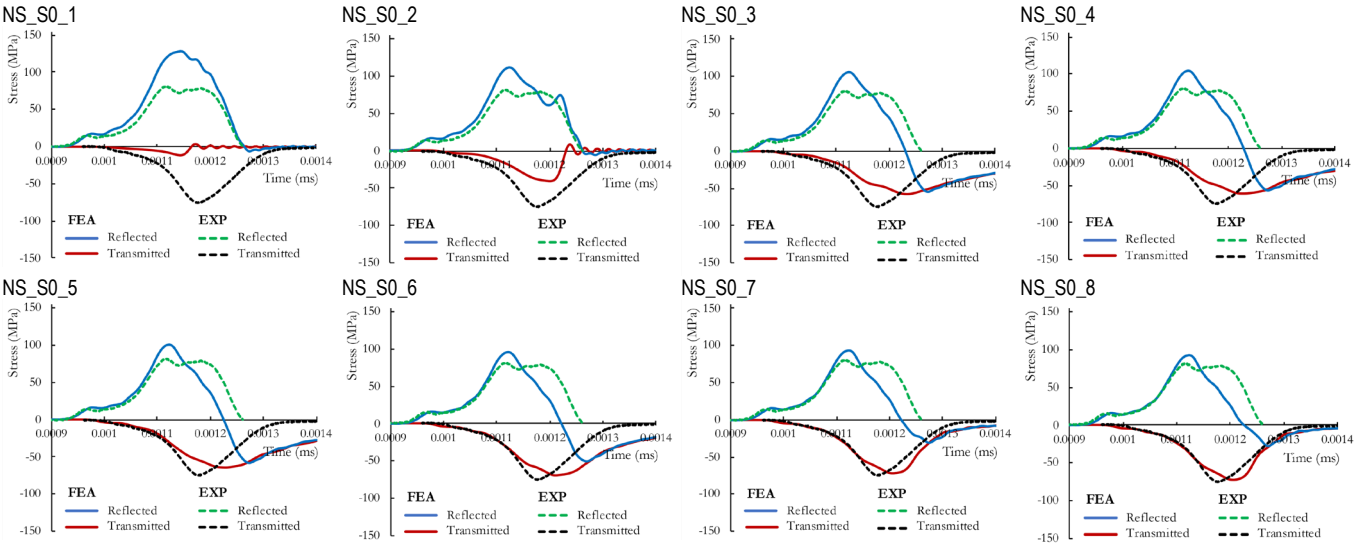

Fig. 6. Waveform data for FEM modelling of the sandstone in the SHPB test: influence of *SFS/SFM* using the NS standard contact definition (*SOFT* = 0)

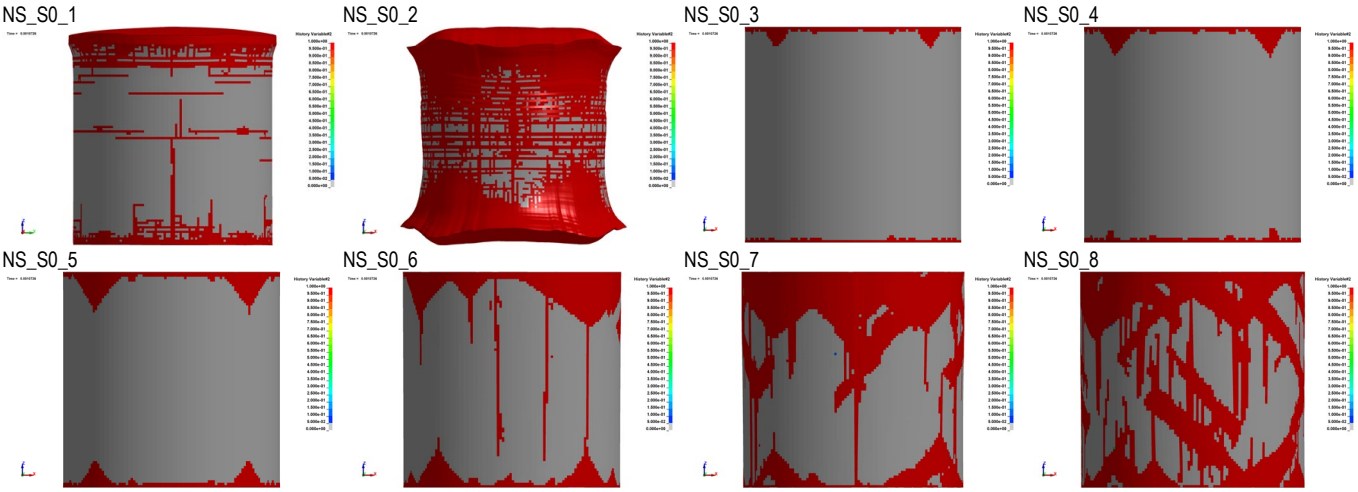

Fig. 7. Specimen failure patterns for FEM modelling of the sandstone in the SHPB test: influence of *SFS/SFM* using the NS standard contact definition (*SOFT* = 0)

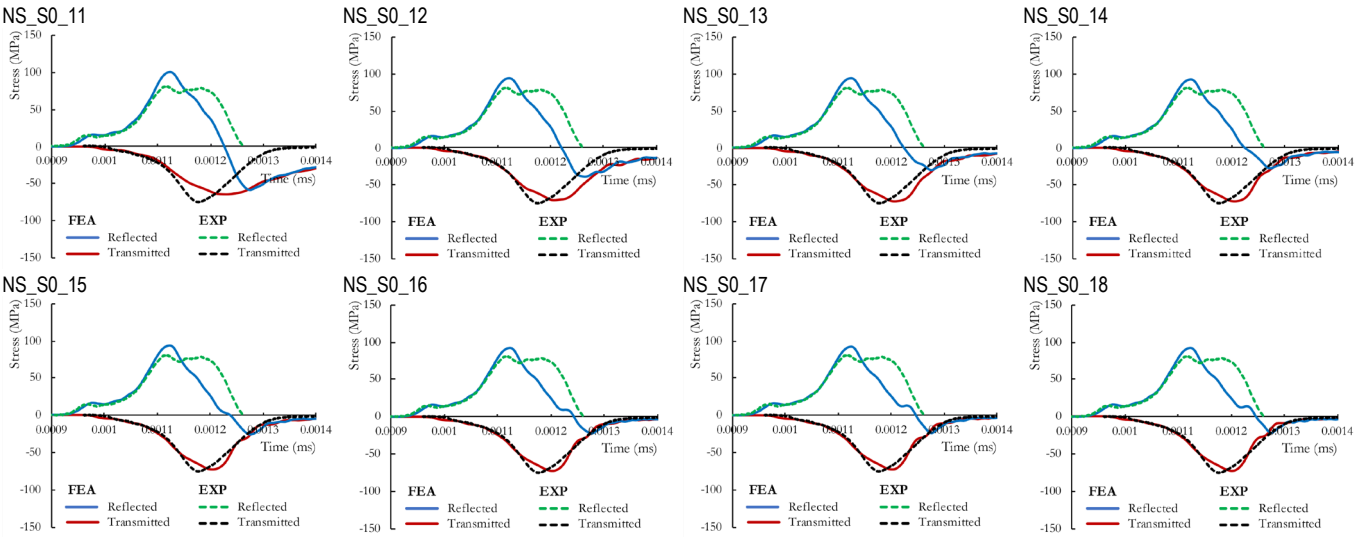

Fig. 8. Waveform data for FEM modelling of the sandstone in the SHPB test: influence of *SLSFAC* using the NS standard contact definition (*SOFT* = 0)

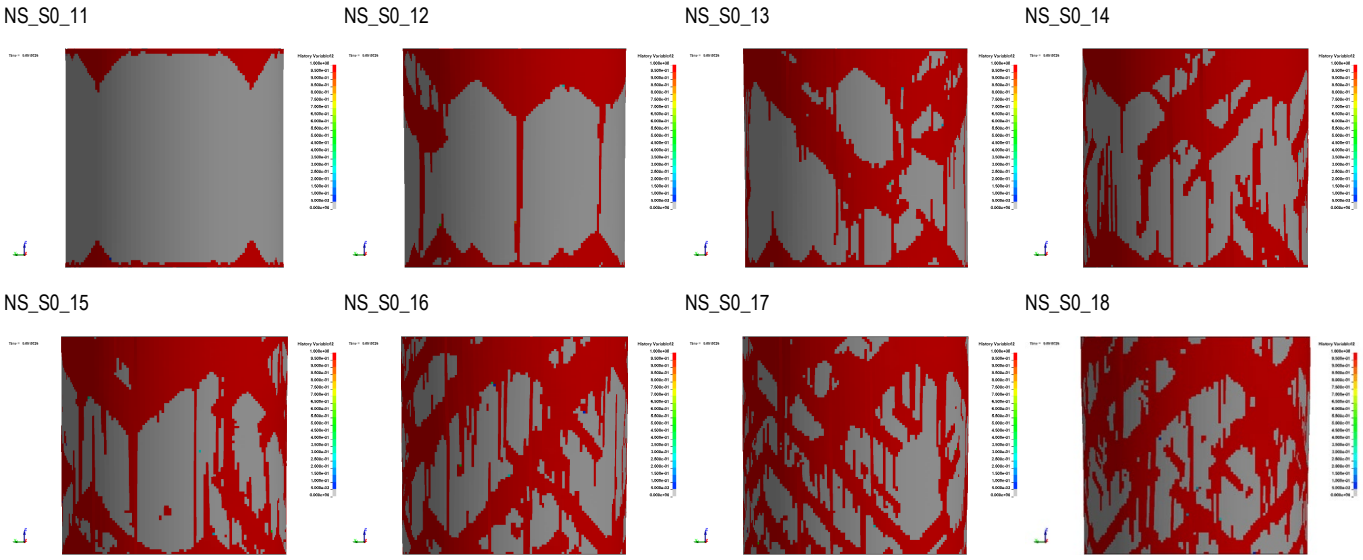

Fig. 9. Specimen failure patterns for FEM modelling of the sandstone in the SHPB test: influence of *SLSFAC* using the NS standard contact definition (*SOFT* = 0)

3.2.3. SPH: NS contact with SOFT = 1

Results of the numerical simulation using the meshless technique for different values of the *SOFTSCL* parameter are shown in Fig. 10 and 11, presenting waveform data and specimen failure pattern, respectively. It can be seen that both waveforms and failure patterns are similar to those obtained with FEM. Again, the stress response over time for different *SOFTSCL* values does not change drastically. Differences arise in the shape of transmitted wave, but they are not significant and can be treated as negligible.

The deformation and failure pattern of the specimen are similar to the high-speed camera photos shown in Fig. 3d. The incline and longitudinal cracks were satisfactorily reproduced in the numerical simulations. It must be noted, though, that deformation of the samples is slightly different in comparison with FEM because the sample had already lost cohesion and its fragments had started to move separately. The character of a transmitted wave generated with the use of SPH is comparable with that obtained with FEM, but the shape of the reflected wave is slightly different. It exhibits a raise of stress in the second part. This behaviour is also connected with better representation of decohesion in the SPH domain. In the FEM, damage is represented by erosion parameters and not real loss of material integrity. As was mentioned, this approach causes an artificial energy dampness In SPH, after decohesion, energy can still be transmitted to other parts of the sample via contact between fragments of this sample.

The difference between the highest and the lowest values of maximum contact force is 10.5%.

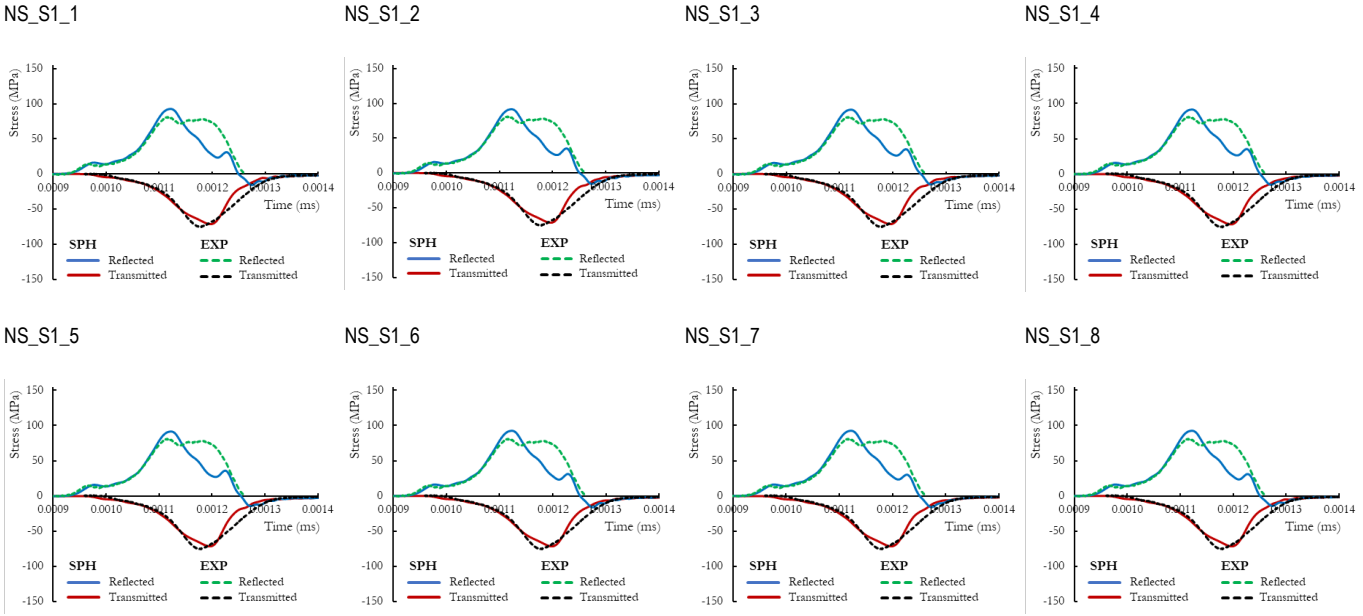

Fig. 10. Waveform data for SPH modelling of the sandstone in the SHPB test: influence of *SOFSCL* using the *SOFT* =1 in the NS contact definition

DOI 10.2478/ama-2024-0029

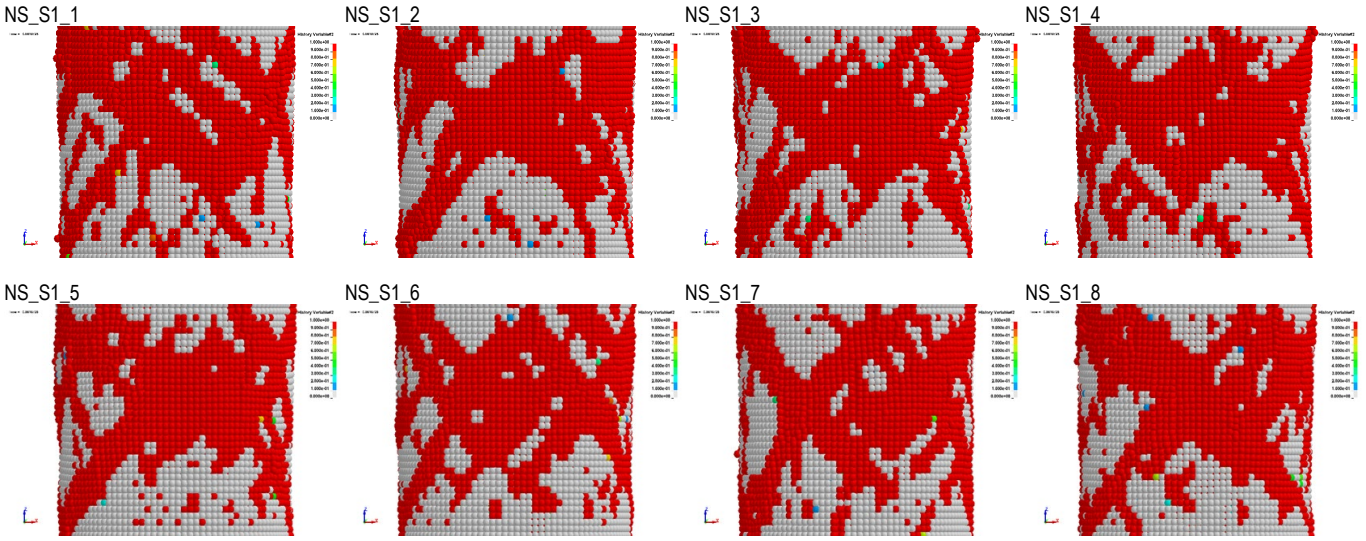

Fig. 11. Specimen failure patterns for SPH modelling of the sandstone in the SHPB test: influence of *SOFTSCL* using the *SOFT* =1 in the NS contact definition

3.2.4. SPH: NS contact with SOFT = 0

Results of the numerical simulation using the meshless technique for different values of the *SFM/SFS* parameter and stiffness estimation set to *SOFT* = 0 are shown in Fig. 12 and 13. Similar to the case with FEM-based simulations, the influence of *SFM/SFS* parameters controlling contact stiffness is significant. It is seen both in the values of maximum contact forces and in the failure patterns. The contact force varies from 59 kN to 95 kN. For the lowest contact force, the algorithm did not converge. For the next lowest value (see case NS_S0_2) there is no failure of the sample. The impact force was too small due to insufficient contact stiffness between the specimen and the bars.

The following analyses show that failure zone (red areas) is increasing when *SFM/SFS* is increasing. For the value of 2.0 of parameter *SFS/SFM* (case NS_S0_6) and above, failure patterns start to be similar to those observed in the experiment, which indicates that the values of contact forces acting on the sample are big enough to obtain acceptable results of numerical simulations.

On the waveform charts it can be seen that for low values of contact forces, the difference between numerical solutions and experiments is significant. Starting from the default value of *SFM/SFS* = 1.0, numerically obtained waveforms better reflect experimental stress history. On the reflected side, for lower contact forces values, there is no additional pick on the right side of the chart. This additional pick of stress can be observed for *SFM/SFS* equal to 1.0 or more.

Results of analyses made with SPH for parameter *SOFT* = 0 and different *SLSFAC* values are presented in Fig. 14 and 15. Overall, the influence of *SLSFAC* is similar to the one observed in case of the first set of tests (change of *SOFTSCL* parameter and contact stiffness estimation set to *SOFT* = 1). The pic values of contact force are also similar to the results obtained in first set of tests and vary from 94.1 kN to 95.6 kN; it is thus unsurprising that failure patterns and stress responses over time are also comparable.

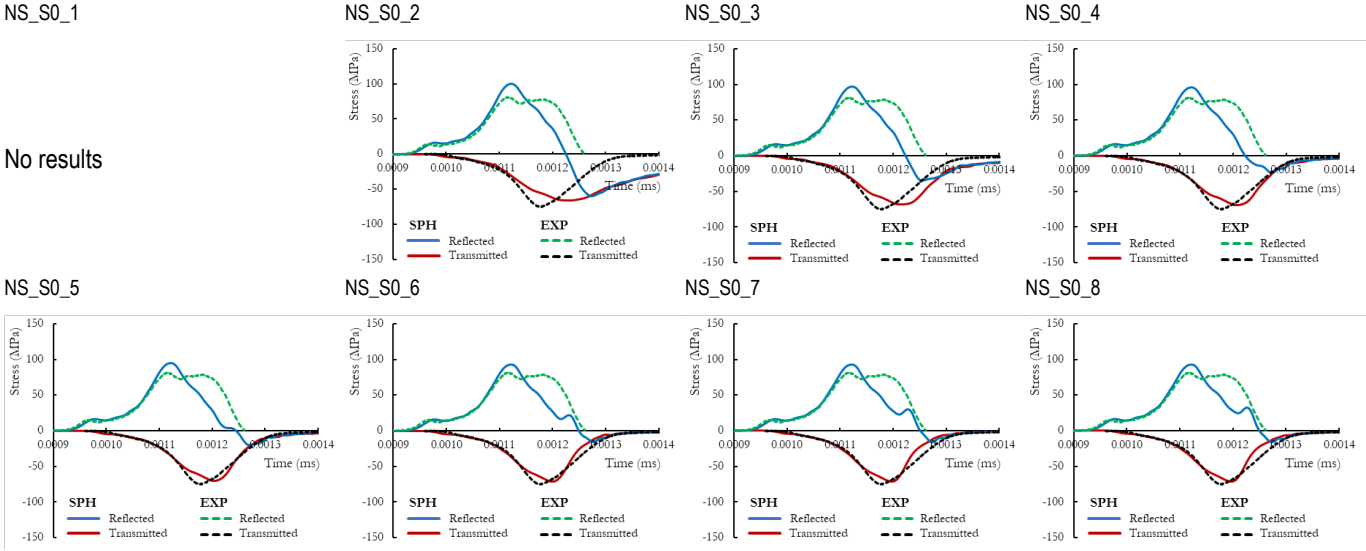

Fig. 12. Waveform data for SPH modelling of the sandstone in the SHPB test: influence of *SFS/SFM* using the NS standard contact definition (*SOFT* = 0)

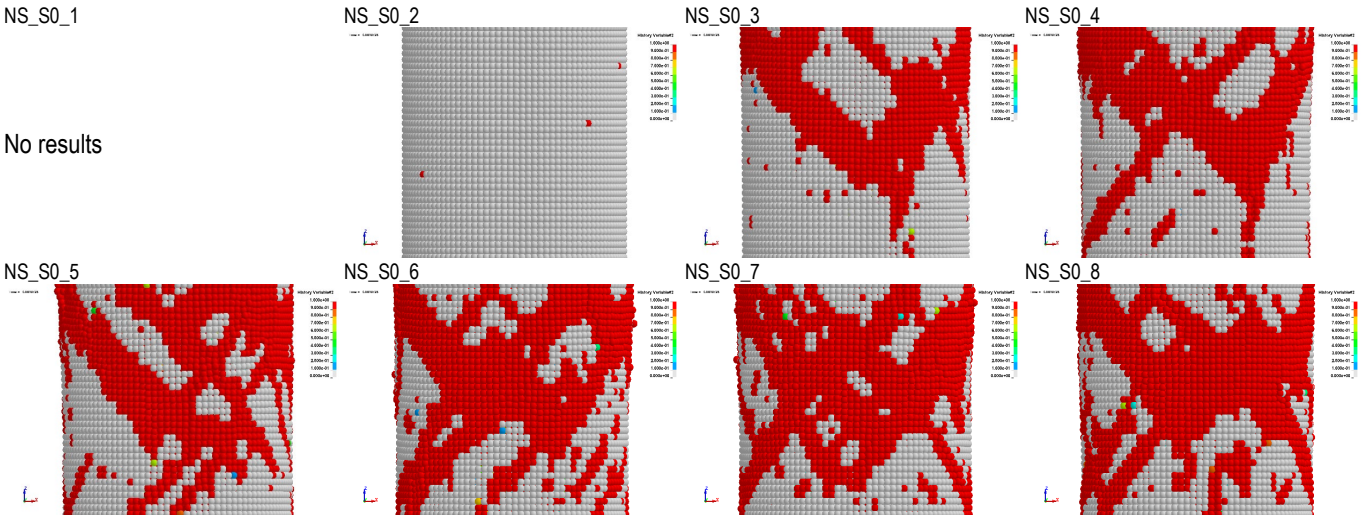

Fig. 13. Specimen failure patterns for FEM modelling of the sandstone in the SHPB test: influence of *SFS/SFM* using the NS standard contact definition (*SOFT* = 0)

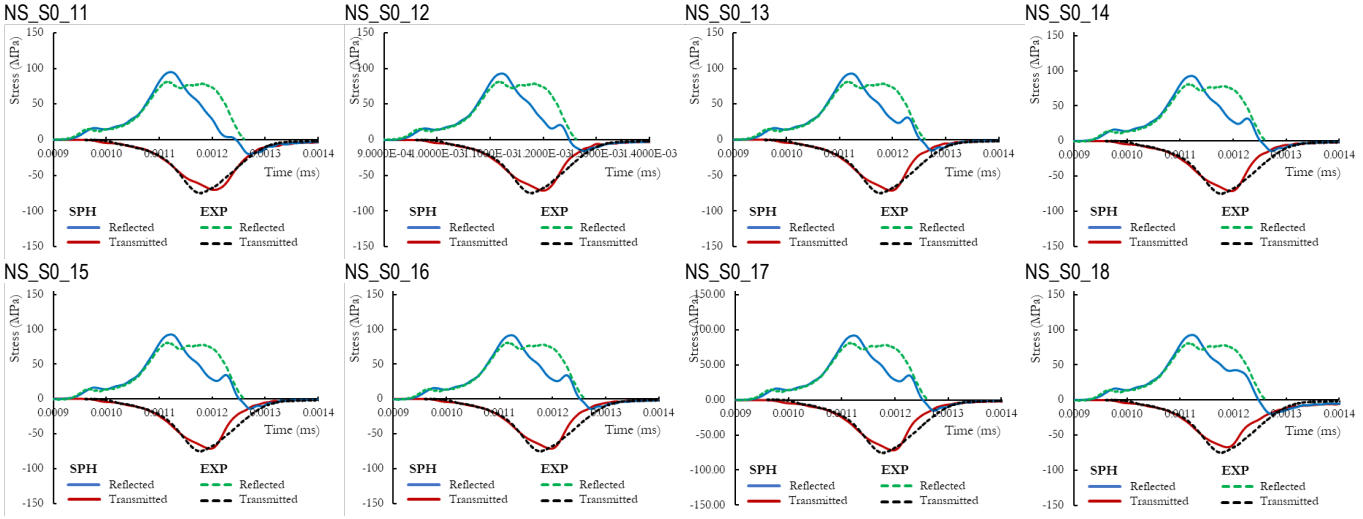

Fig. 14. Waveform data for SPH modelling of the sandstone in the SHPB test: influence of *SLSFAC* using the NS standard contact definition (*SOFT* = 0)

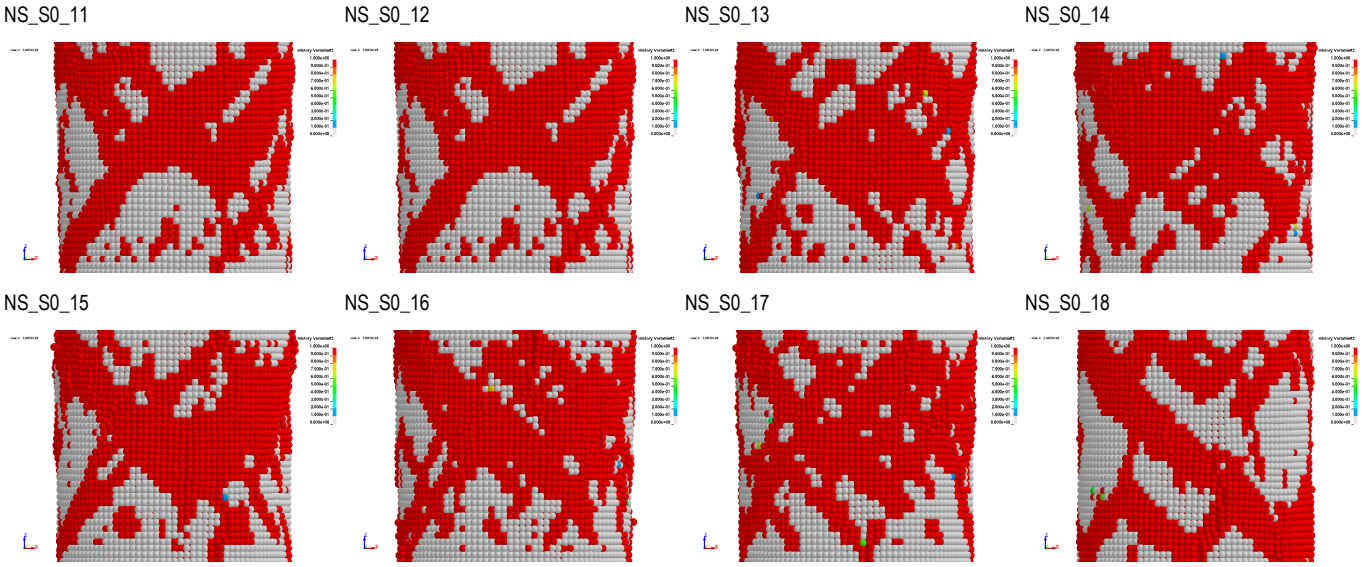

Fig. 15. Specimen failure patterns for SPH modelling of the sandstone in the SHPB test: influence of *SLSFAC* using NS standard contact definition (*SOFT* = 0)

DOI 10.2478/ama-2024-0029

3.3. Two-way contact (SS)

The SS contact was only studied with the specimen modelled using finite elements. For this stage, *SOFT* = 1, *SOFT* = 0 and *SOFT* = 2 with different contact stiffness were considered and have been discussed in the following sections.

3.3.1. FEM: SS contact with SOFT = 1

Changing the contact procedure from NS to SS did not have an influence on the obtained results. The waveform data (Fig. 16) as well as failure patterns (Fig. 17) are nearly identical when both the types of contact were implemented (see **Błąd! Nie można odnaleźć źródła odwołania.** and **Błąd! Nie można odnaleźć źródła odwołania.** with NS for comparison). Insignificant differences in the latter parts of the reflected and transmitted curves were observed between the SS and NS in the corresponding cases. The specimens exhibited very similar failure with two-way contact compared to their counterpart with NS contact definition. Eventually, *SOFT* = 1 provides a practically identical response of the specimen in the SHPB simulation while using one-way and two-way contact treatments.

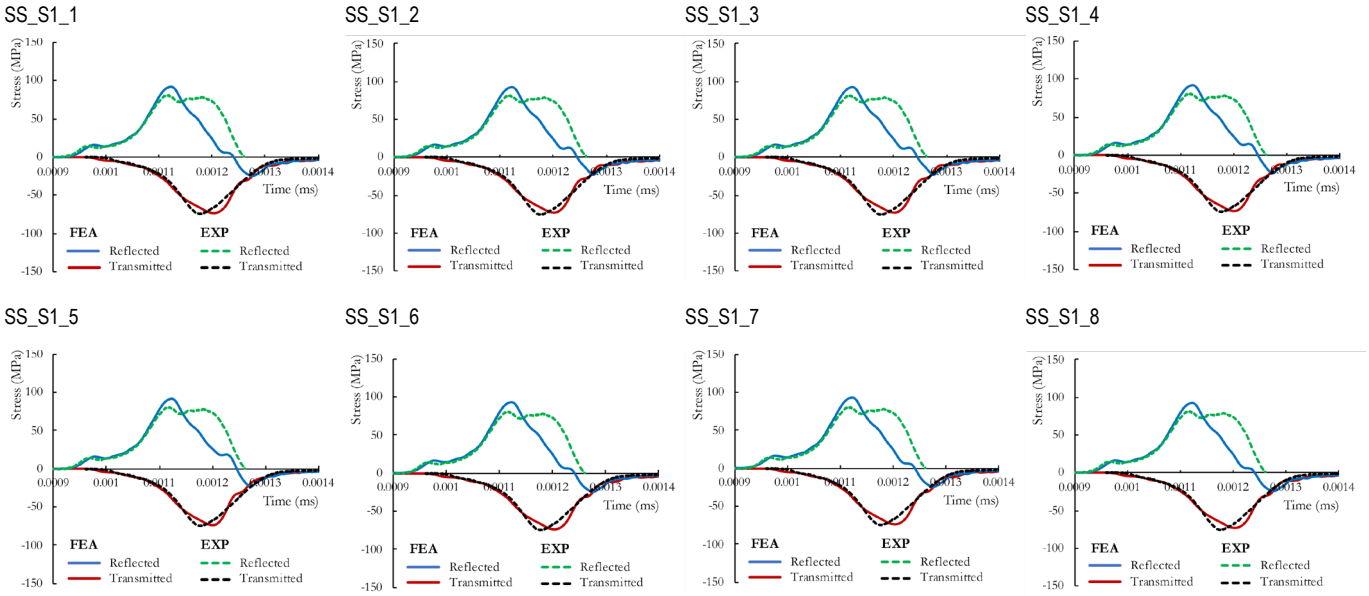

Fig. 16. Waveform data for FEM modelling of the sandstone in the SHPB test: influence of *SOFTSCL* using the *SOFT* = 1 in the SS contact definition

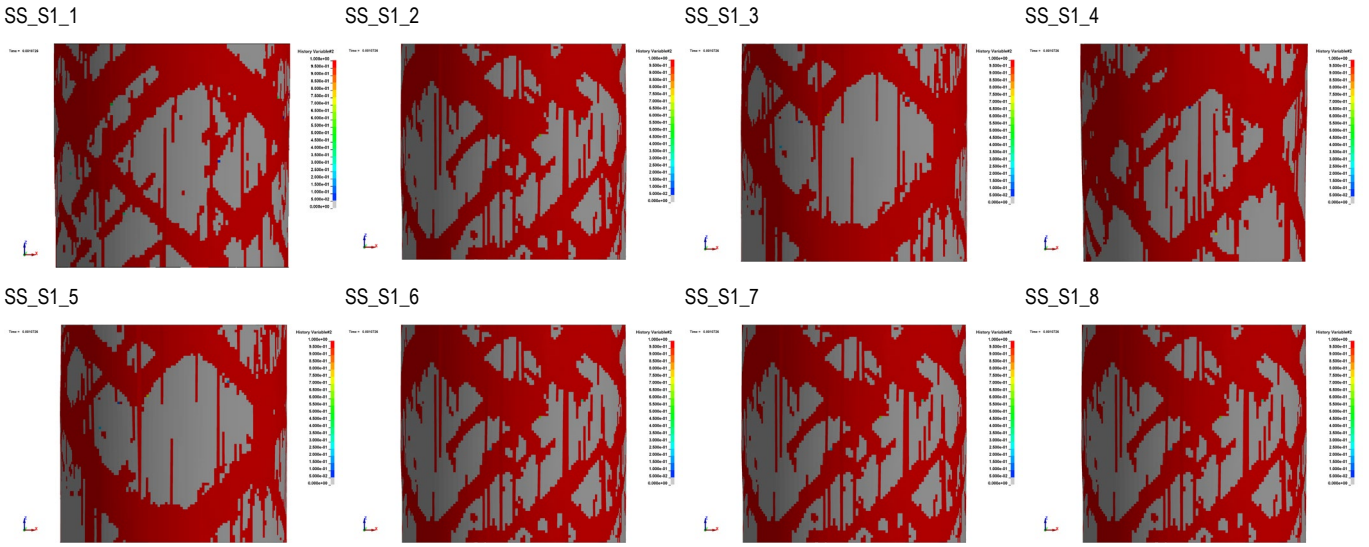

Fig. 17. Specimen failure patterns for FEM modelling of the sandstone in the SHPB test: influence of *SOFTSCL* using the *SOFT* =1 in the SS contact definition

3.3.2. FEM: SS contact with SOFT = 0

When *SOFT* = 0 was adopted for the SS contact, similar observations were also derived compared to the NS contact, with the same algorithm calculating the contact stiffness (see Section 3.2.2). In Fig. 18 and Fig. 19, the transmitted and reflected waves, and failure patterns of the specimen for different values of SFM/SFS with SS and *SOFT* = 0 parameters, respectively, are presented. The influence of parameters controlling contact stiffness can be clearly observed, with significant differences between *FEA* and experiments visible in the first six cases. Especially in the first two tests, the stiffness of contact was too small, resulting in inappropriate transfer of elastic wave in the specimen. From the tested cases, only the last one gave outcomes similar to those associated with the experimental results, but still the reflected wave was not reproduced for its whole length, with an underestimation after the first peak compared to the real-world measurement.

The failure patterns presented in Fig. 19 demonstrate the influence of a different contact stiffness. The incorrect waveform data observed in the first two cases is also demonstrated as an unphysical specimen behaviour with the unsymmetrical failure patterns. The boundary effects near the contact surfaces are noticeable. For the case with *SFS/SFM* = 0.7, longitudinal cracks started to form, and when the contact stiffness increased, additional incline cracks were also observed. By comparison, for the cases using NS contact, cracks were visible only when *SFS/SFM* > 2. Ultimately, the failure pattern was reproduced quite well for the SS_S0_8 case. However, changing the contact from one-way (see

Fig. 7) to two-way did not have an effect on the damage accumulation within the specimen boundaries and edges, which is the unphysical phenomena, especially since the lubricant and polyester foil were used between the specimen and the bars in the experiment.

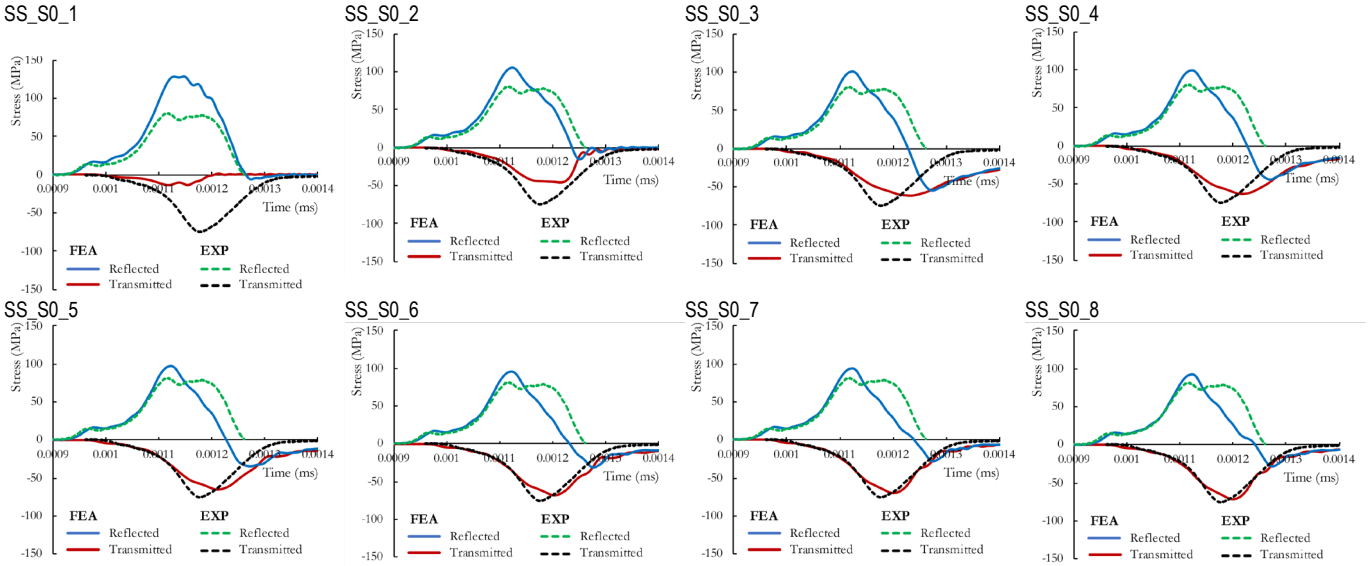

Fig. 18. Waveform data for FEM modelling of the sandstone in the SHPB test: influence of *SFS/SFM* using the *SOFT* = 0 in the SS contact definition

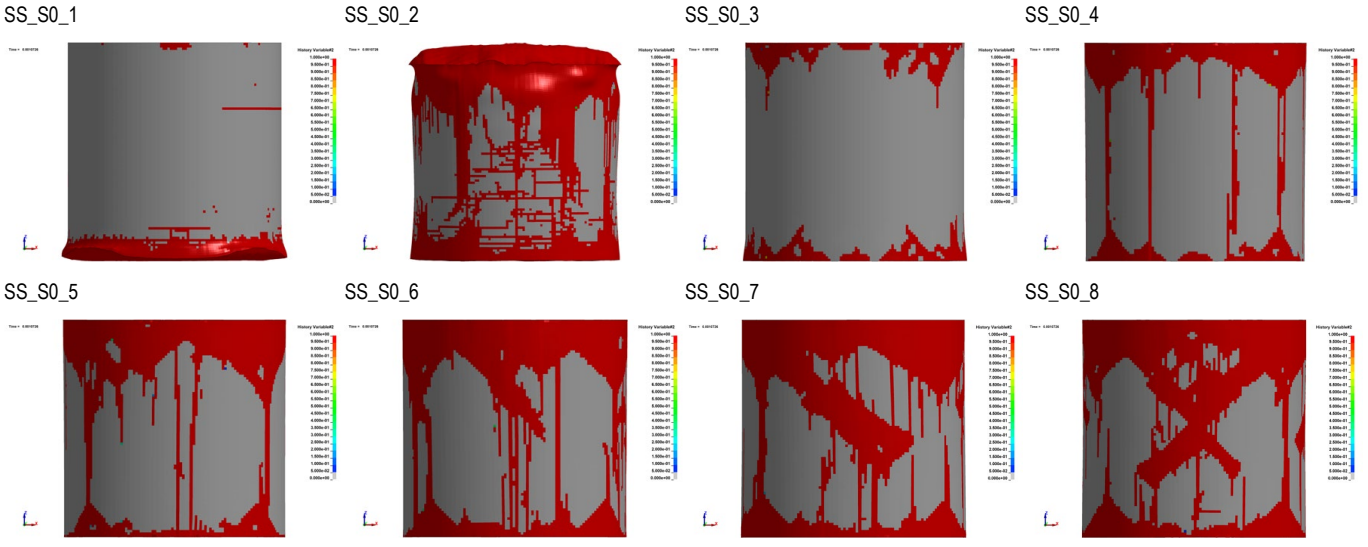

Fig. 19. Specimen failure patterns for FEM modelling of the sandstone in the SHPB test: influence of *SFS/SFM* using the *SOFT* = 0 in the SS contact definition

In the second part of the SS standard contact definition parametric study, different values of *SLSFAC* were changed according to Tab. 4. The waveform data are presented in Fig. 20. For the smallest contact stiffness, the waveform data were not reproduced well by the model, but a general trend is noticeable. Increasing contact stiffness resulted in a better reproduction of the reflected and transmitted curves, and for the SS_S0_16, the best correlation with the experimental outcomes was obtained. Nevertheless, the maximum strength of the material is underestimated (stress peak in the transmitted curve). In the simulations with SLSFAC = 5.0 and SLSFAC = 7.0, the reflected curves were closer to the experimental counterpart, but the material strength was too small. Such phenomenon was not observed for the SFS/SFM study (see Fig. 18), or when the NS contact definition was set in the simulations (see

Fig. 8). The failure patterns are presented in Fig. 21. For the first four cases, only the longitudinal cracks are noticeable, and the boundaries effects had a pronounced effect on the observed damage accumulation in the specimen material. After exceeding *SLSFAC* = 1.0, the incline cracks were formed, and the best reproduction of the cracking characteristics was observed for the SS_S0_16 with *SLSFAC* = 2.0. The boundary effect was not so pronounced in this case compared to the other simulations when *SOFT* = 0 was used. Further increase of the contact stiffness resulted in the unsymmetrical response (SS_S0_17) and numerical instability (SS_S0_18).

In summary, the SS contact with *SOFT* = 0 ultimately allowed satisfactory results to be obtained, while simulating the *FEM* specimen behaviour in the *SHPB* test. However, in this case, SFS/SFM stiffness parameters should be considerably large enough to obtain accurate results when *SLSFAC* has a default value. On the other hand, caution should be taken when SLSFAC is modified, since too large a value can produce an unpredictable and unphysical specimen response.

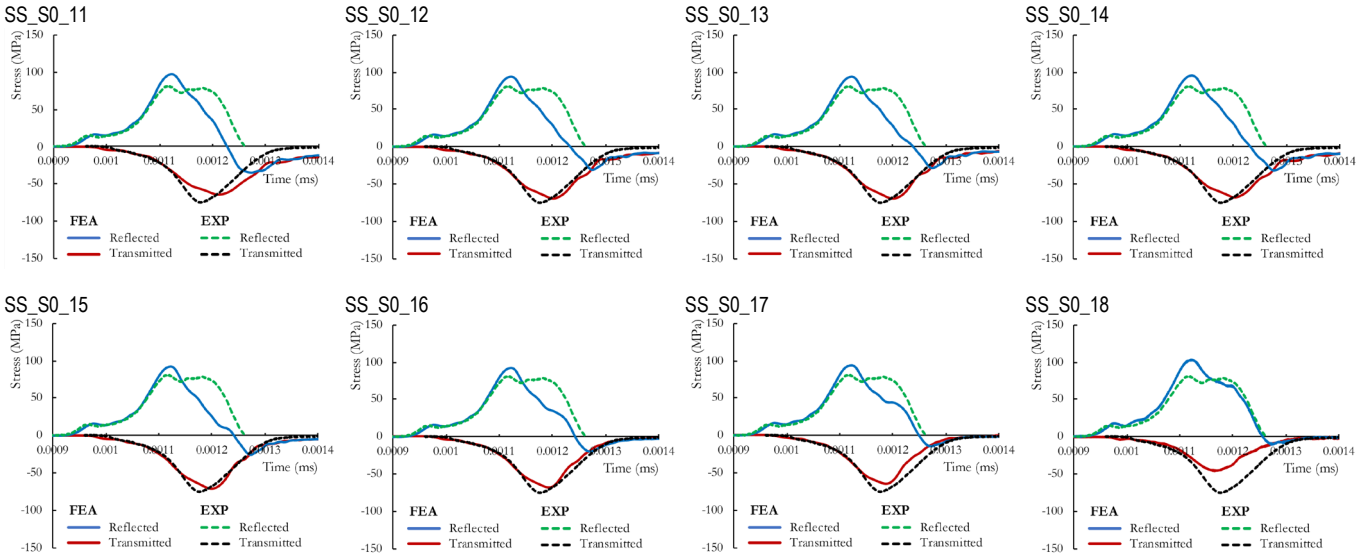

Fig. 20. Waveform data for FEM modelling of the sandstone in the SHPB test: influence of *SLSFAC* using the *SOFT* = 0 in the SS contact definition

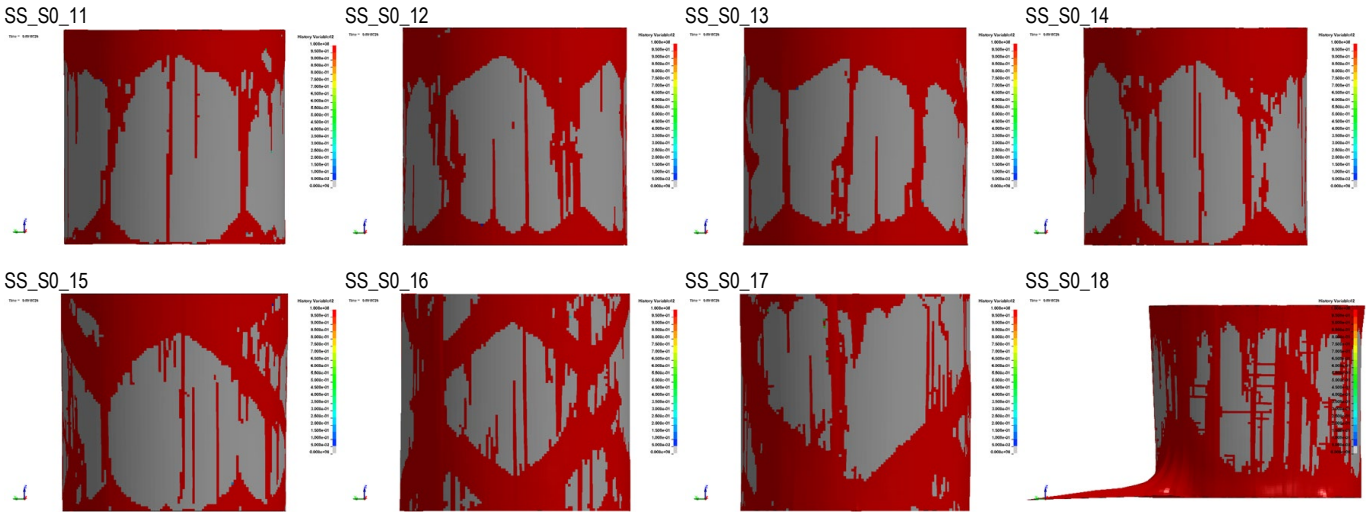

Fig. 21. Specimen failure patterns for FEM modelling of the sandstone in the SHPB test: influence of *SLSFAC* using the *SOFT* = 0 in the SS contact definition

DOI 10.2478/ama-2024-0029

3.3.3. FEM: SS contact with SOFT = 2

In the last stage of the present study, *SOFT* = 2 was used. This option was not adopted in the NS contact since it is only working with a two-way contact procedure, which uses segments of the interacting parts. When *SOFT* = 2 is enabled, *SFS/SFM* and *SLSFAC* parameters influence the contact stiffness.

When different values of *SFS/SFM* were adopted (Fig. 22), considerably better results were obtained compared to the SS contact with *SOFT* = *0*. On the other hand, a larger influence of the *SFS/SFM* parameters was obtained compared to the SS contact with *SOFT* = *1* and *SOFSCL*. The SS_S2_1 to SS_S2_4 gave the worst reproduction of the waveform data, while the transmitted and reflected curves were closer to the experiments from SS_S2_5 to SS_S2_8. The qualitative analysis of the specimen behaviour and failure patterns corresponds to the qualitative comparison of the measured pulses (Fig. 23). The first three cases differ from the other five, which are nearly identical despite different values of *SFS/SFM*. The worst failure pattern was obtained for the first case, when a value of 0.1 was used for *SFS/SFM*.

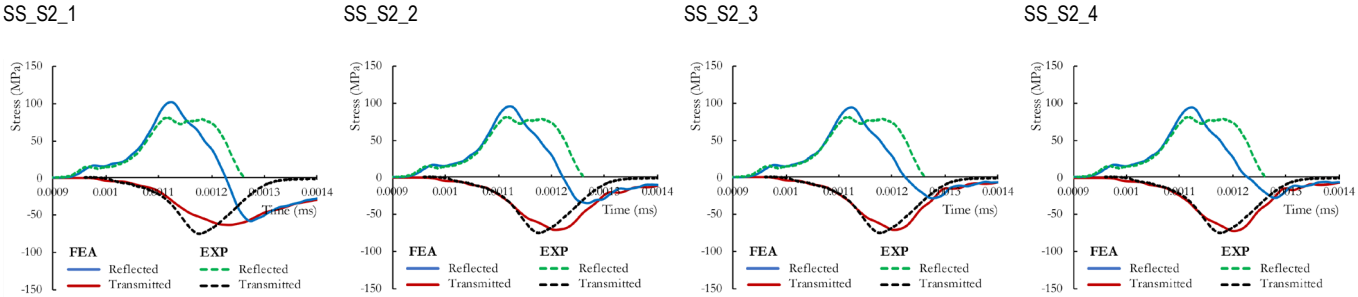

Fig. 22. Waveform data for FEM modelling of the sandstone in the SHPB test: influence of *SFS/SFM* using the *SOFT* = 2 in the SS contact definition

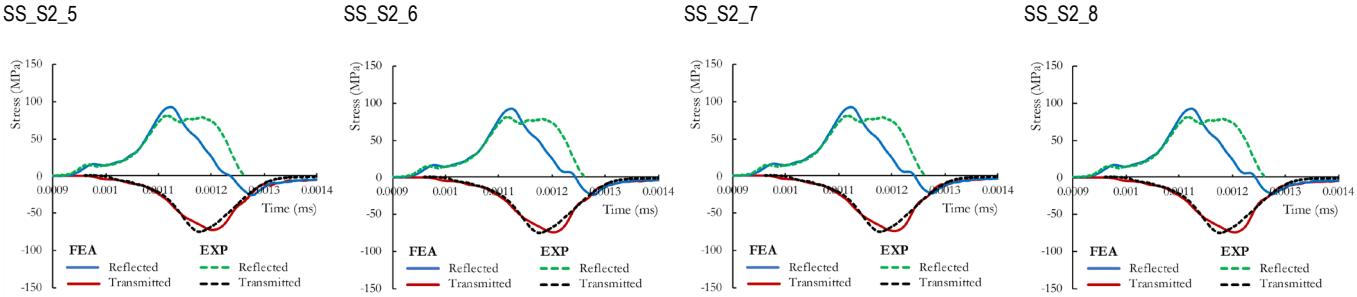

Fig. 22.1. Waveform data for FEM modelling of the sandstone in the SHPB test: influence of *SFS/SFM* using the *SOFT* = 2 in the SS contact definition

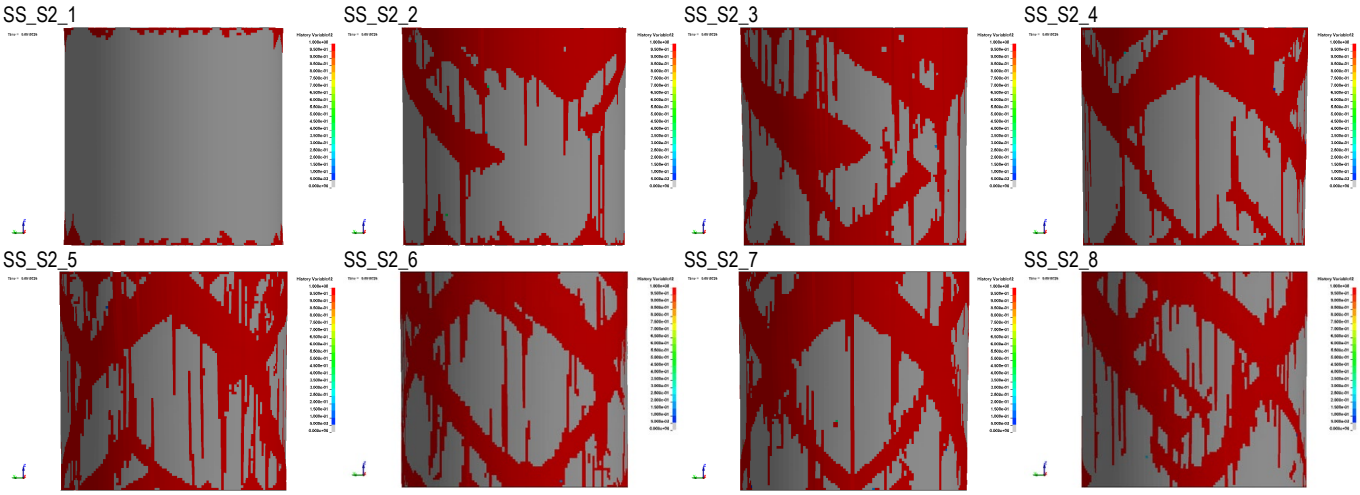

Fig. 23. Specimen failure patterns for FEM modelling of the sandstone in the SHPB test: influence of *SFS/SFM* using the *SOFT* = 2 in the SS contact definition

DOI 10.2478/ama-2024-0029

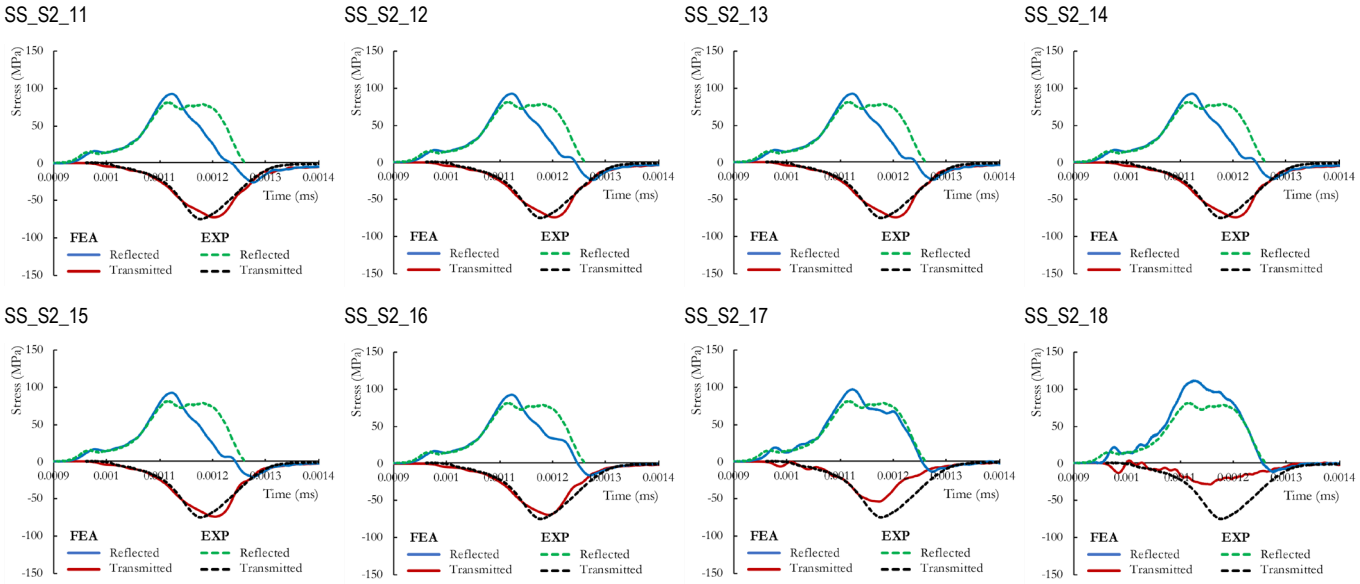

Fig. 24. Waveform data for FEM modelling of the sandstone in the SHPB test: influence of *SLSFAC* using the *SOFT* = 2 in the SS contact definition

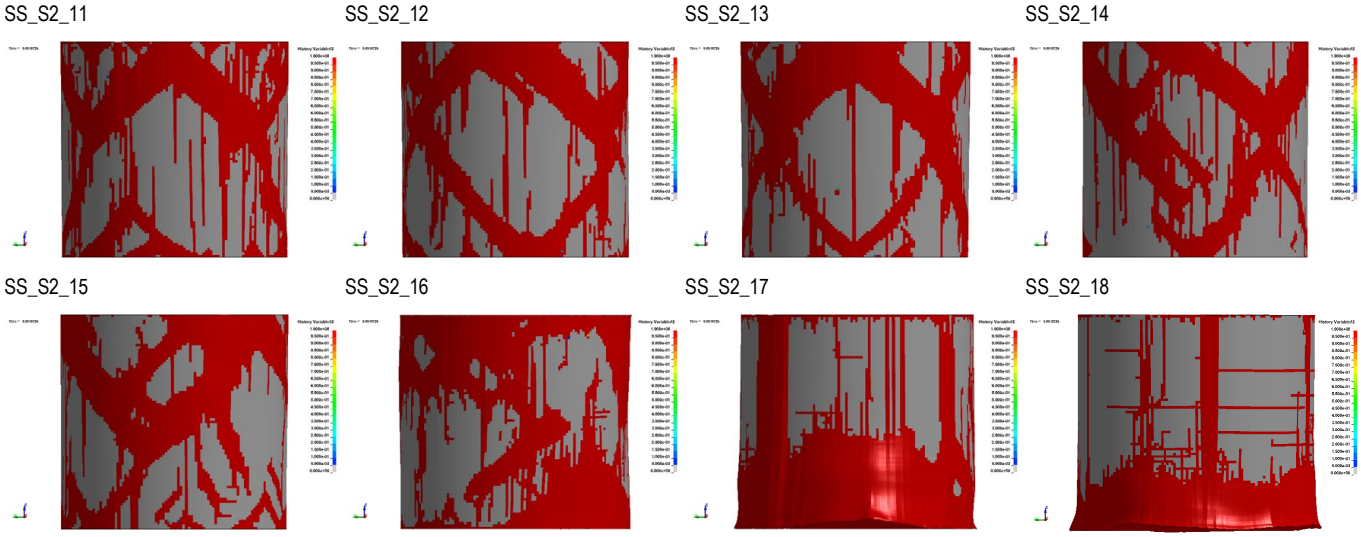

Fig. 25. Specimen failure patterns for FEM modelling of the sandstone in the SHPB test: influence of *SLSFAC* using the *SOFT* = 2 in the SS contact definition

During the last stage of the present study, an analysis of the *SOFT* = *2* formulation is performed with the use of various *SLSFAC* values. Starting from the lowest value of *SLSFAC,* better reproduction of the waves is noticeable, and the most similar data were obtained for the SS_S2_16 case (Fig. 24). Compared to the previous six cases, the reflected waves produced in the last two simulations demonstrated the greatest similarity vis-à-vis the experimental counterparts, but on the other hand, the transmitted waves were not quite well-reproduced and unstable results were observed. The discussed results with the parametric studies using *SLSFAC* for *SOFT* = *2* are nearly consistent with *SOFT* = *0* (see Fig. 20) with very slight differences. The best outcomes were obtained for the SS_S2_16 case. The correspondent failure patterns were relatively close to the real-world observations with inclines and vertical cracks visible in the four first cases (Fig. 25). However, after exceeding the *SLSFAC* = 1, the model was observed to be characterised by unstable behaviour. It is further noteworthy to mention that, despite a relatively good reproduction of the waveform data for SS_S2_16 case, the failure pattern was not acceptable. The worst reproduction of the specimen behaviour was observed for the last two cases, and this development was also consistent with the corresponding results obtained with the use of *SOFT* = *0* (see Fig. 21).

Similarly to the SS contact with *SOFT* = 0, it possible to obtain relatively well-reproduced specimen behaviour and waveform data. However, a user should be cautious since values of *SFS/SFM* stiffness parameters that are too small can produce insufficient contact force, while instability of the model can be observed when too large a value of *SLSFAC* is used.

3.4. General discussion of results

In general, the waveform data are captured well by the FEM, the SPH and the JH-2 constitutive model. For the transmitted curve, both the rise times and peak values are very close to the

laboratory results. However, a slightly more brittle failure can be observed for the numerical simulations compared to the experiment. In the case of reflected waves, the post-peak parts of the curves are not similar. These observations are consistent with previous studies (27, 42, 72) and the main reasons for such discrepancies are: no numerical erosion implementation, homogeneous treatment of the specimen or the mesh being too coarse. Furthermore, fully damaged elements representing the material failure and cracks do not sufficiently reproduce wave effects, and consequently, the reflected wave characteristic is not captured satisfactorily. On the other hand, the deformation and failure pattern of the specimen are similar to the high-speed camera photos shown in Fig. 3d. The incline and longitudinal cracks were satisfactorily reproduced in the numerical simulations.

It can be stated that the NS contact with a default *SOFT* = 0 should be used with caution or should be omitted when interacting materials have significantly different stiffness. Certainly, relatively satisfactory results can be achieved, but the contact stiffness value should be tuned-up in parallel with the constitutive model parameters. This applies both to FEM and SPH.

In the case of both FEM and SPH, NS contact with *SOFT* = 1 provides a relatively good reproduction of the waveform data and failure pattern and is not especially sensitive to the change of the other scaling parameters.

It is possible to obtain satisfactory simulation results using SS kinematics and the *SOFT* = 2 penalty force algorithm, but this would require a careful selection of the scaling parameters. In both investigated scenarios (change of *SFS/SFM* and change of SLSFAC), the results vary from acceptable to the non-physical or even diverging solution.

To better compare numerical results with experimental data, the compressive strength of the sample was verified. This allowed also an evaluation of the contact force values with respect to the quality of the obtained results. Indicative evaluation of failure pattern is also added for better presentation of overall quality of numerical results. Tab. 5–7 contain values for NS contact with FEM, NS contact with SPH and SS contact with FEM, respectively.

For different contact parameters, the pick contact force varies from 57.1 kN to 97.7 kN. It can be noticed that to obtain acceptable results this value must be greater than 95 kN (of course this specific value is connected with the material of sample, and for different materials, the contact force required to produce quality results will be different). Thus, regardless of the other contact options, the *SOFT* = 1 algorithm of deriving contact stiffness gives the highest contact forces and the best correlation with experimental results. Furthermore, this approach is not very sensitive to adjustment of contact stiffness. Therefore, based on the presented studies, it is suggested to use *SOFT* = 1 when simulating the test of rock materials tested on the SHPB apparatus.

Tab. 5. Results from SHPB simulations using FEM and NS contact

Test No.	Exp. compressive strength [MPa]	Num. compressive strength [MPa]	Relative error [%]	FEM contact force [kN]	Failure pattern* [-]
NS_S1_1	75.5	73.7	–2.4	97.4	5
NS_S1_2		73.7	–2.4	97.7	5
NS_S1_3		73.6	–2.5	97.7	5
NS_S1_4		73.7	–2.4	97.7	5
NS_S1_5		73.5	–2.6	97.4	5
NS_S1_6		73.7	–2.4	97.4	5
NS_S1_7		73.7	–2.4	97.3	5
NS_S1_8		73.7	–2.4	97.3	5
NS_S0_1	75.5	11.6	–84.6	19.6	1
NS_S0_2		41.2	–45.5	57.1	1
NS_S0_3		57.2	–24.2	75.4	2
NS_S0_4		60.7	–19.6	79.9	2
NS_S0_5		64.3	–14.8	84.7	2
NS_S0_6		69.3	–8.2	90.9	3
NS_S0_7		71.9	–4.6	94.4	4
NS_S0_8		72.6	–3.7	95.3	5
NS_S0_11	75.5	64.3	–14.8	84.7	2
NS_S0_12		70.8	–6.2	92.6	3
NS_S0_13		72.0	–4.6	94.4	3
NS_S0_14		72.6	–3.8	95.4	4
NS_S0_15		72.8	–3.5	95.9	4
NS_S0_16		73.3	–2.8	96.1	5
NS_S0_17		73.5	–2.6	97.4	5
NS_S0_18		73.6	–2.5	97.5	5

*5 = excellent, 4 = very good, 3 = good, 2 = poor, 1 = instability.

Tab. 6. Results from SHPB simulations using SPH and NS contact

Test no.	Exp. compressive strength [MPa]	Num. compressive strength [MPa]	Relative error [%]	SPH contact force [kN]	Failure pattern* [-]
NS_S1_1	75.5	71.4	–5.4	94.8	5
NS_S1_2		71.4	–5.4	94.7	5
NS_S1_3		71.5	–5.2	95.4	5
NS_S1_4		71.5	–5.2	94.9	5
NS_S1_5		71.5	–5.2	95.4	5
NS_S1_6		71.4	–5.4	94.9	5
NS_S1_7		71.4	–5.4	94.8	5
NS_S1_8		71.4	–5.4	94.9	5
NS_S0_1	75.5	12.1	–83.9	58.7	1
NS_S0_2		65.7	–13.0	83.4	2
NS_S0_3		68.4	–9.4	88.1	3
NS_S0_4		69.7	–7.8	90.7	4
NS_S0_5		70.3	–6.8	92.2	4
NS_S0_6		70.9	–6.1	94.1	5
NS_S0_7		71.4	–5.4	94.3	5
NS_S0_8		71.5	–5.3	95.2	5
NS_S0_11	75.5	70.3	–6.8	92.2	4
NS_S0_12		71.3	–5.5	94.9	5

NS_S0_13		71.4	–5.4	95.1	5
NS_S0_14		71.4	–5.4	95.3	5
NS_S0_15		71.5	–5.2	95.4	5
NS_S0_16		71.6	–5.1	95.6	5
NS_S0_17		71.7	–5.0	90.1	4
NS_S0_18		67.1	–11.1	94.1	5

*5 = excellent, 4 = very good, 3 = good, 2 = poor, 1 = instability.

Tab. 7. Results from SHPB simulations using FEM and SS contact

Test no.	Exp. compressive strength [MPa]	Num. compressive strength [MPa]	Relative error [%]	FEM contact force [kN]	Failure pattern* [-]
SS_S1_1	75.5	73.4	–2.6	97.0	5
SS_S1_2		73.6	–2.4	97.6	5
SS_S1_3		73.7	–2.3	97.6	5
SS_S1_4		73.5	–2.5	97.5	5
SS_S1_5		73.4	–2.6	97.0	5
SS_S1_6		73.3	–2.8	96.9	5
SS_S1_7		73.4	–2.6	97.0	5
SS_S1_8		73.5	–2.5	97.5	5
SS_S0_1	75.5	13.9	–81.6	20.5	1
SS_S0_2		45.9	–39.1	60.2	1
SS_S0_3		60.8	–19.4	80.2	1
SS_S0_4		62.9	–16.7	82.9	2
SS_S0_5		64.8	–14.1	85.2	2
SS_S0_6		67.8	–10.1	89.1	3
SS_S0_7		70.5	–6.6	92.7	4
SS_S0_8		71.3	–5.5	93.8	4
SS_S0_11	75.5	64.8	–14.1	85.2	3
SS_S0_12		69.2	–8.3	90.1	3
SS_S0_13		70.5	–6.6	92.7	3
SS_S0_14		68.0	–9.8	89.3	3
SS_S0_15		71.8	–4.9	94.6	3
SS_S0_16		68.9	–8.6	91.4	4
SS_S0_17		65.0	–13.8	86.5	2
SS_S0_18		45.6	–39.6	59.5	1
SS_S2_1	75.5	63.7	–15.5	84.0	2
SS_S2_2		70.3	–6.9	92.0	3
SS_S2_3		71.3	–5.5	93.5	4
SS_S2_4		71.8	–4.8	94.3	4
SS_S2_5		72.3	–4.2	95.1	5
SS_S2_6		73.6	–2.5	97.2	5
SS_S2_7		74.2	–1.7	97.9	5
SS_S2_8		74.3	–1.5	98.0	5
SS_S2_11	75.5	72.3	–4.2	95.1	5
SS_S2_12		73.6	–2.5	97.2	5
SS_S2_13		74.2	–1.7	97.9	5
SS_S2_14		74.3	–1.5	98.0	5
SS_S2_15		74.3	–1.5	98.0	4
SS_S2_16		69.1	–8.5	91.4	3
SS_S2_17		53.3	–29.3	70.5	1
SS_S2_18		28.7	–61.9	37.7	1

*5 = excellent, 4 = very good, 3 = good, 2 = poor, 1 = instability.

4. CONCLUSIONS

The present study provides numerical simulations of the SHPB dynamic compression test of sandstone sample, aiming to demonstrate the influence of contact procedure parameters on the results with special attention placed on the failure pattern. Based on the obtained results, the following conclusions can be drawn:

- Differences in contact modelling lead to completely different results of the SHPB test simulation, including divergent solutions or unphysical failure patterns. Therefore, the importance attributed to achieving mastery over contact modelling needs to be on a par with that to constitutive modelling, especially in the case of the SHPB test, where the only load acting on the specimens arises from contact/impact, resultant to which verification of the performance of the contact procedure assumes a high degree of importance.
- The nodes to surface (one-way contact) and SS (two-way contact) procedures work well for both FEM and SPH when *SOFT* = 1 is used. In these cases it was possible to obtain results accurately reflecting both data waves and failure patterns.
- With the use of *SOFT* = 0 (default value), generally incorrect results, up to the numerically unstable solutions, were observed despite the added correction of contact stiffness. Utilisation of *SOFT* = 2 requires a number of tests to ascertain the set of parameters that would enable the obtaining of reasonable results.
- Default contact parameters, i.e., those set by the software provider, were also found to give wrong outcomes (see the NS_S0_5 and SS_S0_5 cases), since they resulted in underestimated contact force value.
- Evaluation of waveform data, failure patterns and pick values of stresses is required to efficiently correlate and validate the numerical model, including the constitutive model of a brittle material. Focussing on merely one of these aspects can result in some of the erroneous simulations going unnoticed.

– Finally, the conducted tests indicate the prevalence of an advantage for SPH over FEM in the modelling of sandstone failure in the SHPB test. This is attributable to the fact that the meshless technique can better represent decohesion of the material and thus does not affect the energy balance in the sample during the dynamic compression test to as great an extent as takes place in FEM.

REFERENCES

1. Y. GH, Scott T, W. SP. Concrete Slab Damage and Hazard from Close-In Detonation of Weaponized Commercial Unmanned Aerial Vehicles. J Struct Eng [Internet]. 2021;147(11):4021190. Available from: https://doi.org/10.1061/(ASCE)ST.1943-541X.0003158
2. Morka A, Kędzierski P, Muzolf P. Optimization of the structure of a ceramic-aluminum alloy composite subjected to the impact of hard steel projectiles. Mech Compos Mater. 2016;52(3):333–46.
3. Kędzierski P, Morka A, Sławiński G, Niezgoda T. Optimization of two-component armour. Bull Polish Acad Sci Tech Sci. 2015;63(1): 173–9.
4. Wang J, Yin Y, Esmaieli K. Numerical simulations of rock blasting damage based on laboratory-scale experiments. J Geophys Eng. 2018;15(6):2399–417.
5. Liu K, Wu C, Li X, Li Q, Fang J, Liu J. A modified HJC model for improved dynamic response of brittle materials under blasting loads. Comput Geotech [Internet]. 2020;123(December 2019):103584. Available from: https://doi.org/10.1016/j.compgeo.2020.103584
6. Simons EC, Weerheijm J, Sluys LJ. A viscosity regularized plasticity model for ceramics. Eur J Mech A/Solids. 2018;
7. Johnson GR, Holmquist TJ. Response of boron carbide subjected to large strains, high strain rates, and high pressures. J Appl Phys. 1999;85(12):8060–73.
8. Holmquist TJ, Johnson GR, Cook WH. A computational constitutive model for concrete subjected to large strains, high strain rates, and high pressures. In: The 14th international symposium on ballistic. Quebec: Arlington, VA: American Defense Preparedness Association. 1993; 591–600.
9. Mardalizad A, Caruso M, Manes A, Giglio M. Investigation of mechanical behaviour of a quasi-brittle material using Karagozian and Case concrete (KCC) model. J Rock Mech Geotech Eng. 2019.
10. Pająk M, Janiszewski J, Kruszka L. Laboratory investigation on the influence of high compressive strain rates on the hybrid fibre reinforced self-compacting concrete. Constr Build Mater. 2019;227: 116687.
11. Sucharda O, Pajak M, Ponikiewski T, Konecny P. Identification of mechanical and fracture properties of self-compacting concrete beams with different types of steel fibres using inverse analysis. Constr Build Mater [Internet]. 2017;138:263–75. Available from: http://dx.doi.org/10.1016/j.conbuildmat.2017.01.077
12. Máca P, Sovják R, Konvalinka P. Mix design of UHPFRC and its response to projectile impact. Int J Impact Eng. 2014;63:158–63.
13. Sovják R, Vavřiník T, Zatloukal J, Máca P, Mičunek T, Frydrýn M. Resistance of slim UHPFRC targets to projectile impact using in-service bullets. Int J Impact Eng. 2015;76:166–77.
14. Sielicki PW, Łodygowski T. Masonry wall behaviour under explosive loading. Eng Fail Anal. 2019;104:274–91.
15. Wu H, Qin, Zhang YD, Gong ZM, Wu H, Fang Q, et al. Semi-theoretical analyses of the concrete plate perforated by a rigid projectile. Acta Mech Sin. 2012;28(6):1630–43.
16. Wang Z liang L, Li Y chi C, Shen RF. Numerical simulation of tensile damage and blast crater in brittle rock due to underground explosion. Int J Rock Mech Min Sci. 2007;44(5):730–8.
17. Mazurkiewicz Ł, Damaziak K, Małachowski J, Baranowski P. Parametric study of numerically modelled delamination process in a composite structure subjected to dynamic loading. Eng Trans. 2013;61(1):15–31.
18. Mazurkiewicz Ł, Małachowski J, Baranowski P. Optimization of protective panel for critical supporting elements. Compos Struct. 2015;134:493–505.
19. Peng Y, Wu H, Fang Q, Liu JZ, Gong ZM. Flat nosed projectile penetrating into UHP-SFRC target: Experiment and analysis. Int J Impact Eng. 2016;93:88–98.
20. Liang X, Wu C. Meso-scale modelling of steel fibre reinforced concrete with high strength. Constr Build Mater [Internet]. 2018;165:187–98. Available from: https://doi.org/10.1016/j.conbuildmat.2018.01.028
21. Wu H, Li YC, Fang Q, Peng Y. Scaling effect of rigid projectile penetration into concrete target: 3D mesoscopic analyses. Constr Build Mater. 2019;208:506–24.
22. Liu Z, Zhang C, Zhang C, Gao Y, Zhou H, Chang Z. Deformation and failure characteristics and fracture evolution of cryptocrystalline basalt. J Rock Mech Geotech Eng. 2019;11(5):990–1003.
23. Lv TH, Chen XW, Chen G. The 3D meso-scale model and numerical tests of split Hopkinson pressure bar of concrete specimen. Constr Build Mater. 2018;160:744–64.
24. Wang J, Yin Y, Luo C. Johnson–Holmquist-II(JH-2) Constitutive Model for Rock Materials: Parameter Determination and Application in Tunnel Smooth Blasting. Appl Sci. 2018 Sep 16;8(9):1675.
25. Kang HM, Kang MS, Kim MS, Kwak HK, Park LJ, Cho SH. Experimental and numerical study of the dynamic failure behavior of rock materials subjected to various impact loads. In: WIT Transactions on the Built Environment. WITPress; 2014;357–67.
26. Li XB, Hong L, Yin TB, Zhou ZL, Ye ZY. Relationship between diameter of split Hopkinson pressure bar and minimum loading rate under rock failure. J Cent South Univ Technol.2008;15(2):218–23.
27. Pająk M, Baranowski P, Janiszewski J, Kucewicz M, Mazurkiewicz Ł, Łaźniewska-Piekarczyk B. Experimental testing and 3D meso-scale numerical simulations of SCC subjected to high compression strain rates. Constr Build Mater. 2021;302.
28. Zhang J, Wang Z, Yang H, Wang Z, Shu X. 3D meso-scale modeling of reinforcement concrete with high volume fraction of randomly distributed aggregates. Constr Build Mater. 2018;164:350–61.
29. Zhang X, Hao H, Ma G. Dynamic material model of annealed soda-lime glass. Int J Impact Eng. 2015;77:108–19.
30. Ruggiero A, Iannitti G, Bonora N, Ferraro M. Determination of Johnson-holmquist constitutive model parameters for fused silica. EPJ Web Conf. 2012;26:04011.
31. Hao Y, Hao H, Zhang XH. Numerical analysis of concrete material properties at high strain rate under direct tension. Int J Impact Eng. 2012;39(1):51–62.
32. Xiao J, Li W, Corr DJ, Shah SP. Effects of interfacial transition zones on the stress-strain behavior of modeled recycled aggregate concrete. Cem Concr Res. 2013;52:82–99.
33. Kucewicz M, Baranowski P, Małachowski J. Determination and validation of Karagozian-Case Concrete constitutive model parameters for numerical modeling of dolomite rock. Int J Rock Mech Min Sci. 2020;129.
34. Kucewicz Michaland Baranowski PGR, Małachowski J. Investigation of dolomite'rock brittle fracture using fully calibrated Karagozian Case Concrete model. Int J Mech Sci. 2022;107197.
35. Huang Y, Yang Z, Ren W, Liu G, Zhang C. 3D meso-scale fracture modelling and validation of concrete based on in-situ X-ray Computed Tomography images using damage plasticity model. Int J Solids Struct [Internet]. 2015;67–68:340–52. Available from: http://dx.doi.org/10.1016/j.ijsolstr.2015.05.002
36. Pająk M, Baranowski P, Janiszewski J, Kucewicz M, Mazurkiewicz Ł, Łaźniewska-Piekarczyk B. Experimental testing and 3D meso-scale numerical simulations of SCC subjected to high compression strain rates. Constr Build Mater. 2021;302.
37. Zhang R, Li P yu, Zhi X dong, Wang Y hui, Fan F. Johnson–Holmquist-II model of annealed glass and its verification in dynamic compression test. Structures [Internet]. 2023;53(March):396–407. Available from: https://doi.org/10.1016/j.istruc.2023.04.082
38. Li M, Hao H, Cui J, Hao Y fei. Numerical investigation of the failure

mechanism of cubic concrete specimens in SHPB tests. Def Technol [Internet]. 2022;18(1):1–11.
Available from: https://doi.org/10.1016/j.dt.2021.05.003
39. Ren L, Yu X, Guo Z, Xiao L. Numerical investigation of the dynamic increase factor of ultra-high performance concrete based on SHPB technology. Constr Build Mater [Internet]. 2022;325:126756.
Available from: https://doi.org/10.1016/j.conbuildmat.2022.126756
40. Lv Y, Wu H, Dong H, Zhao H, Li M, Huang F. Experimental and numerical simulation study of fiber-reinforced high strength concrete at high strain rates. J Build Eng [Internet]. 2023;65:105812. Available from: https://doi.org/10.1016/j.jobe.2022.105812
41. Deshpande VM, Chakraborty P, Chakraborty T, Tiwari V. Application of copper as a pulse shaper in SHPB tests on brittle materials- experimental study, constitutive parameters identification, and numerical simulations. Mech Mater [Internet]. 2022;171:104336. Available from: https://doi.org/10.1016/j.mechmat.2022.104336
42. Kucewicz M, Baranowski P, Mazurkiewicz Ł, Małachowski J. Comparison of selected blasting constitutive models for reproducing the dynamic fragmentation of rock. Int J Impact Eng. 2023;173.
43. Johnson GR, Holmquist TJ. An improved computational constitutive model for brittle materials. In AIP Publishing; 2008;981–4.
44. Holmquist TJ, Johnson GR, Grady DE, Lopatin CM, Hertel ES. High strain rate properties and constitutive modeling of glass. In: Mayeless M, Bodner S., editors. Proceedings of 15th International Symposium on Ballistics. Jerusalem, Israel; 1995;234–44.
45. Holmquist TJ, Templeton DW, Bishnoi KD. Constitutive modeling of aluminum nitride for large strain, high-strain rate, and high-pressure applications. Int J Impact Eng. 2001;25(3):211–31.
46. Ai HA, Ahrens TJ. Simulation of dynamic response of granite: A numerical approach of shock-induced damage beneath impact craters. Int J Impact Eng. 2006;33(1–12):1–10.
47. Dehghan Banadaki MM, Mohanty B. Numerical simulation of stress wave induced fractures in rock. Int J Impact Eng. 2012;40–41:16–25.
48. Stanislawek S, Morka A, Niezgoda T. Pyramidal ceramic armor ability to defeat projectile threat by changing its trajectory. Bull Polish Acad Sci Tech Sci. 2015;63(4):843–9.
49. Ruggiero A, Iannitti G, Bonora N, Ferraro M. Determination of Johnson-holmquist constitutive model parameters for fused silica. EPJ Web Conf 26. 2012;04011:1–4.
50. Zhang X, Hao H, Ma G. Dynamic material model of annealed soda-lime glass. Int J Impact Eng. 2015;77:108–19.
51. Baranowski P, Kucewicz M, Gieleta R, Stankiewicz M, Konarzewski M, Bogusz P, et al. Fracture and fragmentation of dolomite rock using the JH-2 constitutive model: Parameter determination, experiments and simulations. Int J Impact Eng. 2020;140:103543.
52. Baranowski P, Kucewicz M, Janiszewski J. JH-2 constitutive model of sandstone for dynamic problems. Submitt to J (under Rev Int J Impact Eng. 2023.
53. Pająk M, Baranowski P, Janiszewski J, Kucewicz M, Mazurkiewicz Ł, Łaźniewska-Piekarczyk B. Experimental testing and 3D meso-scale numerical simulations of SCC subjected to high compression strain rates. Constr Build Mater. 2021;302:124379.
54. Hallquist J. LS-DYNA Theory Manual [Internet]. Vol. 19. Livermore Software Technology Corporation (LSTC); 2019. 886 p. Available from:http://ftp.lstc.com/anonymous/outgoing/jday/manuals/DRAFT_Theory.pdf
55. Kurzawa A, Pyka D, Jamroziak K, Bocian M, Kotowski P. Analysis of ballistic resistance of composites based on EN AC-44200 aluminum alloy reinforced with Al 2 O 3 particles. Compos. Struct.2018;201 :834 –44.
56. Pach J, Pyka D, Jamroziak K, Mayer P. The experimental and numerical analysis of the ballistic resistance of polymer composites. Compos Part B. 2017;113:24–30.
57. Mazurkiewicz Ł, Małachowski J, Tomaszewski M, Baranowski P, Yukhymets P. Performance of steel pipe reinforced with composite sleave. Compos Struct. 2018;183:199–211.
58. Zienkiewicz O, Taylor R, Zhu JZ. The Finite Element Method: its Basis and Fundamentals: Seventh Edition. The Finite Element Method: its Basis and Fundamentals: Seventh Edition. 2013. 1–714 p.
59. Bathe K J. Finite Element Procedures [M] [Internet]. 2005; 1037
Available from:
http://books.google.com/books?id=wKRRAAAAMAAJ&pgis=1%5Cnftp://ftp.demec.ufpr.br/disciplinas/EME748/Textos/Bathe, K.-J. - Finite Element Procedures - 1996 - Prentice-Hall - ISBN 0133014584 - 1052s.pdf
60. Logan D.L. A first course in the finite element method. 5th ed. Cengage Learning; 2010.
61. J. R. An Introduction to the Finite Element Method. 3rd ed. McGraw-Hill Education; 2005.
62. Kleiber M, Breitkopf P. Finite Element Methods in Structural Mechanics: With Pascal Programs. Ellis Horwood; 1993.
63. Gander MJ, Wanner G. From euler, ritz, and galerkin to modern computing. SIAM Rev. 2012;54(4):627–66.
64. Gingold RA, Monaghan JJ. Smoothed particle hydrodynamics: theory and application to non-spherical stars. Mon Not R Astron Soc. 1977;181(3):375–89.
65. Liu GR, Gu YT. An introduction to meshfree methods and their programming. An Introd to Meshfree Methods Their Program. 2005;1–479.
66. Liu MB, Liu GR. Smoothed particle hydrodynamics (SPH): An overview and recent developments. Arch Comput Methods Eng. 2010;17(1):25–76.
67. Gasiorek D, Baranowski P, Malachowski J, Mazurkiewicz L, Wiercigroch M. Modelling of guillotine cutting of multi-layered aluminum sheets. J Manuf Process [Internet]. 2018 Aug;34:374–88. Available from: https://linkinghub.elsevier.com/retrieve/pii/S1526612518307059
68. Baranowski Paweland Janiszewski J, Malachowski J. Study on computational methods applied to modelling of pulse shaper in split-Hopkinson bar. Arch Mech. 2014;66(6):429–52.
69. Wriggers P. Computational contact mechanics. Computational Contact Mechanics. 2006;1–518.
70. Vulović S, Živković M, Grujović N, Slavković R. A comparative study of contact problems solution based on the penalty and Lagrange multiplier approaches. J Serbian Soc Comput Mech. 2007;1(1):174–83.
71. Yastrebov VA. Introduction to Computational Contact. In: Numerical Methods in Contact Mechanics. 2013; 1–14.
72. Kucewicz M, Baranowski P, Małachowski J, Ma J. Determination and validation of Karagozian-Case Concrete constitutive model parameters for numerical modeling of dolomite rock. Int J Rock Mech Min Sci. 2020;129.

DOI 10.2478/ama-2024-0029

This research was supported by the Interdisciplinary Center for Mathematical and Computational Modeling (ICM), University of Warsaw (Grant No. GA73-19) and the ANSYS National License coordinated by ICM UW. The research was also funded by Military University of Technology, Grant No. 22-876. The numerical models were prepared using Altair HyperMesh software. The authors would like to thank Prof. Jacek Janiszewski for conducting experimental research.

Paweł Baranowski: https://orcid.org/0000-0002-5320-9479

Krzysztof Damaziak: https://orcid.org/0000-0002-0439-1606